Numerical simulations of surf zone wave dynamics using Smoothed Particle Hydrodynamics

R. J. Lowe[1,2,3,4], M. L. Buckley[1,4], C. Altomare[5,6], D. P. Rijnsdorp[1,4], Y. Yao[7], T. Suzuki[8,9], J. Bricker[9]

[1] Oceans Graduate School and UWA Oceans Institute, The University of Western Australia, Crawley, Australia
[2] School of Earth Sciences, The University of Western Australia, Crawley, Australia
[3] ARC Centre of Excellence for Coral Reef Studies, The University of Western Australia, Crawley, Australia
[4] Wave Energy Research Centre, The University of Western Australia, Crawley, Australia
[5] Universitat Politècnica de Catalunya – Barcelona Tech, Barcelona, Spain
[6] Ghent University, Ghent, Belgium
[7] Changsha University of Science and Technology, Changsha, China
[8] Flanders Hydraulics Research, Antwerp, Belgium
[9] Dept. of Hydraulic Engineering, Faculty of Civil Engineering and Geosciences, Delft University of Technology, Delft, Netherlands

Corresponding author:

Ryan J. Lowe (Ryan.Lowe@uwa.edu.au)
The University of Western Australia
35 Stirling Hwy, Crawley, Western Australia, Australia

Abstract

In this study we investigated the capabilities of the mesh-free, Lagrangian particle method (Smoothed Particle Hydrodynamics, SPH) to simulate the detailed hydrodynamic processes generated by both spilling and plunging breaking waves within the surf zone. The weakly-compressible SPH code DualSPHysics was applied to simulate wave breaking over two distinct bathymetric profiles (a plane beach and fringing reef) and compared to experimental flume measurements of waves, flows, and mean water levels. Despite the simulations spanning very different wave breaking conditions (including an extreme case with violently plunging waves on an effectively dry reef slope), the model was able to reproduce a wide range of relevant surf zone hydrodynamic processes using a fixed set of numerical parameters. This included accurate predictions of the nonlinear evolution of wave shapes (e.g., asymmetry and skewness properties), rates of wave dissipation within the surf zone, and wave setup distributions. By using this mesh-free approach, the model is able to resolve the critical crest region within the breaking waves, which provided robust predictions of the wave-induced mass fluxes within the surf zone responsible for undertow. Within this breaking crest region, the model results capture how the potential energy of the organized wave motion is initially converted to kinetic energy and then dissipated, which reproduces the distribution of wave forces responsible for wave setup generation across the surf zone. Overall, the results reveal how the mesh-free SPH approach can accurately reproduce the detailed wave breaking processes with comparable skill to state-of-the-art mesh-based Computational Fluid Dynamic models, and thus can be applied to provide valuable new physical insight into surf zone dynamics.

1   Introduction

The accurate prediction of wave transformation and wave breaking in the nearshore zone, including how waves impact coastal structures, remains one of the great challenges in the fields of nearshore oceanography and coastal engineering. Much of this uncertainty stems from how to most accurately simulate the breaking process (i.e., overturning of the free surface), and in turn, how wave transformation within the surf zone region triggers a range of additional nearshore hydrodynamic processes, including additional sources of water level variations (e.g., low frequency waves and wave setup) and wave-driven mean flows. The accurate description of the full range of nearshore water motions is critical to develop robust predictions of wave-driven coastal impacts, including coastal flooding, erosion and storm damage to coastal infrastructure.

2

33   The nonlinear physics that govern nearshore wave transformation (e.g., the cross-shore

34   evolution of wave shape, nonlinear energy transfers, and ultimately dissipation) are especially

35   challenging to predict in practical coastal-scale applications due to the wide range of spatial and

36   temporal scales of the processes involved. For example, both breaking and non-breaking waves

37   drive mass transport over relatively large-scales (i.e., order 10s to 100s of meters); whereas,

38   incident wave energy ultimately becomes dissipated as heat within turbulent flow fields at much

39   finer-scales (i.e., order centimetres or less). Historically, it has been impractical to directly predict

40   (both analytically and numerically) the full spectrum of hydrodynamic processes in the nearshore

41   zone. To fill this gap, experimental observations (both within the lab and field) have been critical to

42   advance process understanding of nearshore hydrodynamics by supporting the development of

43   empirical formulations to parameterize surf zone processes that occur at scales finer than can be

44   resolved by a coastal model. However, as a general rule, a reliance on the parameterization of

45   physical processes within coastal models can risk undermining their predictive benefits; for

46   example, this can require case-specific (non-physical) tuning of empirical parameters to datasets or

47   may cause models to entirely fail when extended to coastal applications and/or or complex study

48   sites beyond the parameter space for which they were initially developed and validated.

49   Nearshore wave models can be broadly placed into two main categories: phase-averaged

50   (spectral) and phase-resolving models. Phase-averaged wave models attempt to simulate the

51   stochastic properties of waves, usually based on linear wave theory, with empirical formulations to

52   parameterize the nonlinear physics (e.g., wave breaking dissipation, wave-wave interactions, etc.).

53   These models are also commonly coupled to flow models to simulate slowly-varying flow

54   properties (i.e., time-scales greater than the wave group envelope period) such as wave setup and

55   mean wave-driven currents. Given that phase-averaged models can only provide crude

56   representations of complex surf zone physics, they often require some degree of parameter tuning to

57   match experimental observations and thus may be incapable of simulating the full range of

58   hydrodynamic processes that are important in a nearshore application. For example, it is relatively

59   common to find that models that have been tuned to optimally reproduce surf zone wave

60   transformation underpredict the magnitude of wave setup, especially when waves break on steep

61   slopes (e.g., Lashley et al., 2018, Skotner and Apelt, 1999). This indicates that these models may

62   not correctly predict the cross-shore distribution of wave forces (radiation stress gradients), which

63   has been attributed to the poor accounting of the conversion of potential to kinetic energy under

64   breaking waves and subsequent dissipation in the inner surf zone (e.g., Buckley et al., 2015). The

65   inclusion of additional empirical formulations (e.g., roller models) have been proposed to account

66   for these unresolved processes during breaking (Svendsen, 1984); however, these approaches have

67 had varying degrees of success and introduce additional model parameters that are not universally

68 applicable across nearshore applications.

69   Phase-resolving wave models, loosely defined here as any wave-flow model that

70 deterministically resolve motions at time-scales shorter than individual sea-swell waves, are

71 designed to include a more complete representation of the nonlinear physics of nearshore waves.

72 Depth-averaged (2DH, two-dimensional in the horizontal) versions of these models (or multi-layer

73 versions employed with coarse vertical resolution) are commonly either Boussinesq-type or based

74 on the nonlinear shallow water equations with non-hydrostatic pressure corrections (commonly

75 referred to as non-hydrostatic wave-flow models). While 2DH phase-resolving models may more

76 accurately simulate the nonlinear behaviour of non-breaking waves in shallow water, they are still

77 incapable of directly resolving the wave breaking process and thus may suffer from some of the

78 same shortcomings as phase-averaged models (i.e., empirical parameterization of the breaking

79 process). Due to their (quasi) depth-averaged description, 2DH models also do not capture the

80 vertical structure of the (mean) flow dynamics (e.g., the undertow profile). Three-dimensional (3D)

81 phase-resolving wave-flow models (summarized below) provide the most rigorous representation of

82 nearshore hydrodynamics, including the capability to directly resolve at least some of the wave

83 breaking process, but are computationally expensive. These models can be classified as either

84 mesh-based or mesh-free. The former class are based on various solutions of Eulerian forms of the

85 (Reynolds-Averaged) Navier-Stokes equations on numerical grids (meshes). The latter class are

86 based on Lagrangian solution of the Navier-Stokes equations, which include those based on particle

87 methods that attempt to describe the motion of a fluid continuum using discrete particles (Liu and

88 Liu, 2003).

89   Several 3D mesh-based approaches have been developed to simulate waves in the nearshore,

90 which mainly differ in their treatment of the free surface. Multi-layered non-hydrostatic wave-flow

91 models (e.g., Zijlema and Stelling, 2008, Bradford, 2010, Ma et al., 2012) describe the free-surface

92 as a single-valued free-surface (akin to 2DH phase-resolving models). Although this simplification

93 allows them to capture the dissipation of breaking waves and 3D flows more efficiently, it also

94 implies that they cannot resolve all details of the breaking process such as wave overturning, and

95 breaking wave-generated turbulence (e.g., Derakhti et al., 2016b, Rijnsdorp et al., 2017).

96 Alternatively, Computational Fluid Dynamic (CFD) models use more comprehensive techniques

97 that can capture complex details of the free surface such as under breaking waves. This includes the

98 marker and cell method (Harlow and Welch, 1965), level-set method (Osher and Sethian, 1988),

99 and Volume Of Fluid (VOF) method (Hirt and Nichols, 1981), of which the VOF approach has

100 been most widely adopted to model nearshore processes (e.g., Torres‑Freyermuth et al., 2007, Yao

101 et al., 2019). Although these models can capture the breaking process and the turbulent flow field in

102 detail, comparisons between laboratory experiments and mesh-based RANS solvers have

103 highlighted some of the difficulties in accurately predicting turbulent flow fields within the surf

104 zone. In particular, model predictions have been shown to be sensitive to the turbulence model used

105 (e.g., Brown et al., 2016), which can lead to a significant discrepancies in undertow profiles

106 predicted throughout the surf zone (e.g., Brown et al., 2016, Larsen and Fuhrman, 2018).

107   The most common mesh-free particle methods are Smoothed Particle Hydrodynamics (SPH)

108 and Moving Particle Semi-implicit (MPS) models. SPH methods (which is the specific focus here),

109 were originally developed as a general numerical approach for supporting continuum mechanics

110 applications, which are now used across a range of scientific fields, including astrophysics, fluid

111 mechanics and solid mechanics (Monaghan, 1992). In more recent years (particularly over the past

112 decade), SPH has become an increasingly common technique applied to coastal and ocean

113 engineering problems, due to its ability to deal with complex geometries, account for highly

114 nonlinear flow behaviour, and to simulate large deformations at interfaces (including moving

115 boundaries and at the free surface) (e.g., Monaghan and Kos, 1999, St-Germain et al., 2013,

116 Altomare et al., 2015b, Crespo et al., 2017, González-Cao et al., 2019, Zhang et al., 2018a,

117 Altomare et al., 2014, Domínguez et al., 2019). Nevertheless, SPH is still being continuously

118 developed and improved; for example, there is still concerted international effort to improve

119 performance related to numerical implementations (including enhancing model convergence,

120 consistency, and stability and adaptivity schemes) and improving treatment of boundary conditions

121 (including at solid boundaries, at the free surface and when coupling to other models). In coastal

122 wave applications, SPH techniques are now being increasingly applied to study wave-structure

123 interactions (including loads and overtopping) (e.g., Akbari, 2017, Altomare et al., 2015a,

124 González-Cao et al., 2019) and the dynamics of floating bodies (e.g., Bouscasse et al., 2013, Ren et

125 al., 2017, Crespo et al., 2017). To a lesser degree, SPH approaches have also been used to

126 investigate the physics of surf zone processes; for example, in recent studies of surf zone currents

127 and eddies (Wei et al., 2017, Farahani et al., 2013), nearshore wave breaking (e.g., Issa and Violeau,

128 2009, Makris et al., 2016, De Padova et al., 2018, Roselli et al., 2019, Shao and Ji, 2006) and surf

129 zone energy balances (Wei and Dalrymple, 2018). Nevertheless, despite the great promise of SPH

130 to nearshore applications, a rigorous assessment of the ability of SPH models to accurately simulate

131 a full range of relevant surf zone hydrodynamic processes is still relatively sparse, certainly in

132 comparison to the wealth of information derived from detailed nearshore wave modelling studies

133 (including mesh-based CFD modelling approaches).

134   In this study, we conduct a detailed investigation of the ability of the SPH modelling

135   approach to predict a broad range of nearshore processes relevant to coastal applications where

136   wave breaking is important. Using experimental data of wave breaking over both a plane beach and

137   a fringing reef profile, we demonstrate how the model can accurately reproduce a broad range of

138   relevant hydrodynamic processes, ranging from the nonlinear evolution of wave shapes across the

139   surf zone, wave setup distributions, and mean current profiles. We compare the present surf zone

140   predictions with predictions by other classes of wave models from literature and illustrate some of

141   the advantages of the SPH approach (particularly in resolving hydrodynamics within the crest

142   region above the wave trough).

143

144   **2   Methods**

145   **2.1 General features of the SPH method**

146   Smoothed Particle Hydrodynamics (SPH) is a mesh-free numerical method where a

147   continuum is discretised into particles. The approach was originally developed within astrophysics

148   (Lucy, 1977, Gingold and Monaghan, 1977) and since then largely applied across a wide range of

149   Computational Fluid Dynamics (CFD) applications. Within SPH, the particles represent calculation

150   nodal points that are free to move in space according to the governing Lagrangian dynamics, such

151   as in fluid mechanics based on the Navier-Stokes equations (Monaghan, 1992). The kinematic and

152   dynamic properties of each particle (e.g., position, velocity, density pressure, etc.) then result from

153   the interpolation of the values of the neighbouring particles. The distance between each *i-th* particle

154   and its neighbours determines the weighting of the contribution of the nearest particles based on

155   application of a weighted kernel function (W). The area of influence of the kernel function is

156   defined using a characteristic smoothing length (h_{SPH}). The kernel function is a finite representation

157   of the Dirac function (i.e., for the limit where h_{SPH} approaches zero), and has a finite distance cut-

158   off (often ± 2 or 3 times h_{SPH}) to avoid contributions (and hence interaction computations) with

159   other particles beyond this distance. While a variety of kernel functions have been proposed for

160   SPH, a Quintic kernel (Wendland, 1995) is often used (including in the present study), where the

161   weighting function vanishes for initial particle spacing greater than $2h_{SPH}$.

162   In general, SPH methods can be grouped into two main classes: Weakly Compressible SPH

163   (WCSPH) and Incompressible SPH (ISPH). A comprehensive review of both the WCSPH and

164   ISPH approaches is presented in Gotoh and Khayyer (2018), which describes the latest

165   developments of both WCSPH and ISPH in terms of stability, accuracy, energy conservation,

166   boundary conditions and simulations of multiphase flows and fluid–structure interactions. The

167 fundamental difference between WCSPH and ISPH is how each method solves for the pressure and

168 density fields. In WCSPH, an appropriate equation of state (i.e., Tait's equation, see below) is

169 solved in a fully-explicit form; whereas Incompressible SPH (ISPH) solves a Poisson pressure

170 equation by applying projection-based methods. The primary advantage of WCSPH is the ability to

171 directly relate pressure and density, rather than having to obtain pressure fields by solving a Poisson

172 equation (as in the case of ISPH) at significant computational expense. As a consequence, WCSPH

173 can be readily parallelized in numerical codes, including on Graphics Processing Units (GPUs) (see

174 below), given that the motion of each particle is solved independently. The WCSPH approach,

175 however, is not without drawbacks (Lee et al., 2008): it can require using very small numerical time

176 steps, and also require using various numerical approaches to avoid model instabilities due to non-

177 physical density / pressure fluctuations that can arise from the compressibility of the flow (see

178 below). For the present work we use a WCSPH solver, so the focus will be on detailing specific

179 aspects of this approach further below.

180   The mathematical foundation of SPH is based around integral interpolants, in which any

181 function $F(\vec{r})$ in coordinate space $\vec{r}$ can be computed by the integral approximation:

$$F(\vec{r}) = \int F(\vec{r}')W(\vec{r} - \vec{r}', h_{SPH})d\vec{r}' \qquad (1)$$

182

183 This function F can be expressed in discrete form based on particles, in which the approximation of

184 the function is interpolated at particle a and the summation is performed over all the particles b that

185 are located within the region of the kernel:

$$F(\vec{r}_a) \approx \sum_b F(\vec{r}_b)W(\vec{r}_a - \vec{r}_b, h_{SPH})\Delta V_b \qquad (2)$$

186

187 where the volume ΔV_b associated with a neighbouring particle b is m_b / ρ_b, where m and ρ are

188 mass and density, respectively. The momentum equation in discrete SPH form for a weakly

189 compressible fluid can then be written as (Monaghan, 1992):

$$\frac{d\vec{u}_a}{dt} = -\sum_b m_b \left(\frac{P_b + P_a}{\rho_b \rho_a} + \Pi_{ab} \right) \nabla_a W_{ab} + \vec{g} \qquad (3)$$

190

191 where t is time, $\vec{u}_a = d\vec{r}_a / dt$ is the velocity of particle a, P is pressure, $\vec{g}$ is gravitational

192 acceleration, and W_{ab} is the kernel function that depends on the distance between particles a and b.

193 The effect of viscous dissipation within SPH can be approximated using the artificial viscosity term

194 Π_{ab} (Monaghan, 1992):

195
$$\Pi_{ab} = \begin{cases} \dfrac{-\alpha \overline{c_{ab}} \mu_{ab}}{\rho_{ab}} & \vec{u}_{ab} \cdot \vec{r}_{ab} < 0 \\ 0 & \vec{u}_{ab} \cdot \vec{r}_{ab} > 0 \end{cases}$$ (4)

196 where $\vec{r}_{ab} = \vec{r}_a - \vec{r}_a$ and $\vec{u}_{ab} = \vec{u}_a - \vec{u}_b$, $\mu_{ab} = h_{SPH} \vec{u}_{ab} \cdot \vec{r}_{ab} / \left(\vec{r}_{ab}^2 + \varepsilon^2 \right)$ with $\varepsilon^2 = 0.01 h_{SPH}$,

197 $\overline{c_{ab}} = 0.5 \left(c_a + c_b \right)$ is the mean speed of sound, and α is a coefficient (termed artificial viscosity) that

198 determines the rate of viscous dissipation. The formulation for Π_{ab} given by Eq. (4) is linearly

199 proportional to velocity gradients and thus produces the effect of a shear and bulk viscosity.

200 Altomare et al. (2015a) proposed using a reference value of $\alpha = 0.01$ for coastal applications, based

201 on model validation against experimental data for wave propagation and induced loading onto

202 coastal structures. Roselli et al. (2018) employed a Multi-Objective Genetic Algorithm to find a set

203 of SPH parameters that led to accurate modelling of wave propagation and found a comparable

204 optimal value for α equal to 0.004. While more sophisticated formulations have been proposed to

205 predict viscous stresses, including Sub-Particle Scale (SPS) turbulence closure models (Gotoh et al.,

206 2004, Dalrymple and Rogers, 2006) that are analogous to Large Eddy Simulation (LES) in CFD

207 applications, in the present study we use the simple artificial viscosity scheme with high particle

208 resolution, which we found led to more robust (stable) model simulations over the range of test

209 cases considered (see section 2.4) with accurate results.

210   In a similar way to Eq. (3), a discrete form of the continuity equation can be expressed as:

211
$$\frac{d\rho_a}{dt} = \sum_b m_b \left(\vec{u}_a - \vec{u}_b \right) \cdot \nabla_a W_{ab}$$ (5)

212 For WCSPH, following Monaghan (1994), pressure and density are related by Tait's equation of

213 state that is expressed as:

214
$$P = B \left[\left(\frac{\rho}{\rho_0} \right)^\gamma - 1 \right]$$ (6)

215 where $\gamma = 7$ is the polytropic constant and $B = c_0^2 \rho_0 / \gamma$ is defined based on the reference density ρ_0

216 and the speed of sound c_0. The equation of state is considered stiff, so oscillations in the density

217 field are allowed within a range of 1% by adjusting the compressibility (and hence the speed of

218 sound) and finding a trade-off between the size of the time step (determined by the Courant

219 condition based on the speed of sound) and the density variations. This is achieved by reducing the

220 speed of sound but maintaining it at least 10 times higher than the maximum velocity in the system

221 to approximate an incompressible flow. Note that while an additional diffusive term is often

8

222 included in Eq. (5) to reduce density fluctuations, such as through incorporation of a δ-SPH

223 formulation (Molteni and Colagrossi, 2009), such approaches can lead to some detachment of the

224 free surface due to truncation of the kernel close to the free surface within breaking waves;

225 therefore, to avoid introducing potential inaccuracies, in the present study we did not use the δ-SPH

226 formulation within the version of DualSPHysics used.

227 Finally, in the SPH framework any number of derived hydrodynamic quantities can be

228 defined and computed. For example, the vorticity $\vec{\omega} = \nabla \times \vec{u}$ (examined later in this study) can be

229 computed for an arbitrary particle i based on gradients computed with surrounding particles j within

230 the compact support domain (Monaghan, 1992):

231
$$\omega_i = \sum_j m_j \left(\vec{u}_i - \vec{u}_j \right) \times \nabla_i W_{ij}. \tag{7}$$

232 **2.2 The DualSPHysics model**

233 The present study uses the open-source solver DualSPHysics (http://dual.sphysics.org/)

234 based on WCSPH (Crespo et al., 2011, Crespo et al., 2015). DualSPHysics is written in two

235 languages, namely C++ and CUDA, and optimized to use the parallel processing power of either

236 CPUs and/or GPUs (Domínguez et al., 2013). GPUs offer greater computing power relative to

237 CPUs, and thus have emerged as an affordable option to accelerate SPH modelling, including

238 making the study of real engineering-scale problems more possible (e.g., Altomare et al., 2014).

239 The governing mass and momentum equations (Eqs. (3) and (5)) were numerically solved

240 within DualSPHysics by integrating in time using a numerically stable two-stage explicit

241 Symplectic method with a variable time step that was functionally dependent on a combination of

242 the Courant–Friedrich–Levy (CFL) condition, the forcing terms and the viscous diffusion term

243 following (Monaghan and Kos, 1999) (see Crespo et al., 2015 for details of the specific

244 implementation). Within SPH, a single (optimum) approach to incorporate solid boundaries in fluid

245 mechanics applications has yet to be established, with improvement of boundary conditions having

246 been specified by the SPH community as a priority research topic, including within the SPHERIC

247 Grand Challenges (http://spheric-sph.org/grand-challenges). In DualSPHysics, the interaction

248 between solid boundaries and fluid particles is solved by employing Dynamic Boundary Conditions

249 (DBCs), as described in Crespo et al. (2007), which provides a very simple yet robust method for

250 incorporating fluid-solid interactions that can be easy to apply, even for very complex geometries.

251 With this approach, solid boundaries consist of a set of particles that are treated as fluid particles but

252 their movement is constrained: the boundaries can be fixed or can move according to a particular

253 forcing or motion time series. The Navier-Stokes equations are then applied to the interactions

254 between boundary and fluid particles, with the only exception that the movement of the boundary

255 particles is prescribed or equal to zero. When a fluid particle approaches a boundary particle, the

256 fluid density locally increases, which in turn generates an increase in the pressure per the equation

257 of state (Eq. (6)) employed in WCSPH. The rise of pressure results in a repulsive force that prevents

258 a fluid particle from passing through the boundary particles. In DualSPHysics the user has the

259 option to apply additional artificial viscosity to the fluid-boundary interaction, which can be used to

260 parameterize drag forces at the boundary (i.e., due to sub-particle-scale bed roughness). As the

261 experiments considered in this study had smooth walls, no boundary enhancement of artificial

262 viscosity was used in the present study.

263 For wave generation, DualSPHysics implements different schemes. Waves can be generated

264 using boundary particles as moving boundaries (MB) that mimic the movement of a wavemaker in

265 a physical facility. Long-crested second-order monochromatic waves, random sea states (including

266 bound long waves) and solitary waves can be automatically generated (Domínguez et al., 2019,

267 Altomare et al., 2017). To absorb the reflected waves at the wavemaker and prevent the introduction

268 of extra spurious energy in the fluid domain, an Active Wave Absorption System (AWAS) has been

269 implemented in DualSPHysics (Altomare et al., 2017). The water surface elevation at the

270 wavemaker position is used and transformed by an appropriate time-domain filter to obtain a

271 control signal that corrects the wave paddle displacement in order to absorb the reflected waves.

272 The position of the wavemaker is obtained in real time through the velocity correction of its motion.

273 As an alternative to MB, waves can be generated in DualSPHysics by enforcing the orbital velocity

274 of the fluid particles in a specific generation area, using a Relaxation Zone method described in

275 (Altomare et al., 2018) or imposing fluid velocity and surface elevation in a buffer zone defined

276 within an open boundary scheme (Verbrugghe et al., 2019a). Finally, coupling with other models

277 can also be employed to generate waves in DualSPHysics (e.g., Altomare et al., 2015b, Altomare et

278 al., 2018, Verbrugghe et al., 2019b): for these applications, the water surface elevation and orbital

279 velocity of SPH fluid particles is derived from other phase-resolving wave models (e.g.,

280 OceanWave3D and SWASH). In the present study, MBs with a piston-type wavemaker are

281 employed.

282 **2.3 Experimental cases**

283 Model performance was assessed using observations from two experimental datasets that

284 include a range of wave conditions and different bathymetry profiles. This study focuses on the

285 hydrodynamics generated by regular (monochromatic) waves, which allows the surf zone processes

286 to be investigated in detail under quasi-steady state conditions with reduced computational times

287   (i.e., simulating order 100 waves versus order 1000 waves to resolve irregular wave statistics). The

288   two experimental datasets comprise (Figure 1): 1) the two test cases of regular wave breaking on a

289   plane beach in Ting and Kirby (1994) (hereafter denoted TK94) that include both 'spilling' and

290   'plunging' wave breaking conditions; and 2) the two test cases reported in Yao et al. (2012)

291   (hereafter Y12) that report regular wave transformation across a reef profile at two still water

292   depths.

Ting and Kirby (1994) – plane beach

294   TK94 obtained detailed measurements of the mean and turbulent flow structures generated

295   by regular wave breaking on a linear-sloping plane beach (note that subsequent analysis of this

296   dataset is also described in Ting and Kirby (1995) and Ting and Kirby (1996)). The wave flume was

297   configured with an initial flat bed (depth h=0.4 m) followed by a beach with 1:35 slope (Figure 1a).

298   'Spilling' breaking waves were generated by incident waves with offshore wave height H=0.125 m

299   and period T=2.0 s; whereas 'plunging' breaking waves were generated by waves of effectively the

300   same height at breaking (H=0.128 m) but with longer period (T=5 s). For both cases, water

301   elevations (η) were recorded using capacitance wave gauges at 100 Hz at ~20 cross-shore

302   locations. Vertical profiles of flow velocities (both horizontal u and vertical w velocity components)

303   were obtained using laser Doppler anemometry (LDA) at 100 Hz at several cross-shore locations (8

304   and 7 locations for the spilling and plunging cases, respectively); note that due to the intermittent

305   wetting / drying and presence of air bubbles during breaking, valid current measurements could not

306   be obtained over the entire crest-to-trough region (only the lower portion). An additional advantage

307   of the TK94 dataset is its historical use to assess the performance of a number of different models,

308   which range from applications using Boussinesq wave models (e.g., Tissier et al., 2012, Cienfuegos

309   et al., 2010), non-hydrostatic RANS models (e.g., Derakhti et al., 2016a, Rijnsdorp et al., 2017,

310   Smit et al., 2013), and mesh-based CFD models such as OpenFOAM (e.g., Jacobsen et al., 2012,

311   Brown et al., 2016), thereby providing an opportunity to place the present SPH simulations in the

312   context of prior studies using other classes of models.

Yao et al. (2012) – fringing reef

314   Y12 describe measurements of wave transformation across a reef profile with a steep (~1:6)

315   sloping forereef and 7 m wide horizontal reef flat located 0.35 m above the wave flume bottom

316   (Figure 1b). At the back of the reef flat, the depth extended again to the bottom of the flume and

317   was followed by a 1:8 beach covered with a porous mat to dissipate wave energy. Note that in the

318   model configuration we treated this beach as a solid boundary as residual wave energy reaching this

319   location was negligible (see below); i.e. effectively all the incident wave energy was dissipated over

320   the reef. We also confirmed that this downstream configuration had effectively no influence on the

11

321 results over the reef, given that initial testing of a reflective vertical wall at the location of the beach

322 had no noticeable effect on any of the results measured across the reef.

323   In this study we focus on two of the test cases described in Y12 (denoted Case 1 and 3 in

324 that study), which used similar regular wave conditions (incident wave heights of H=0.095 m and

325 H=0.101 m, and periods T=1.25 s and 1.00 s for Cases 1 and 3, respectively). The main difference

326 between the cases was the still water level relative to the reef flat: Case 1 had a still-water reef flat

327 depth of h_r=0.1 m, whereas for Case 3 the still water level was at the reef flat level (i.e., h_r=0 m).

328 For both cases, water levels were measured at 50 Hz using 8 resistance-type wave gauges and 4

329 ultrasonic water level sensors. In addition, Yao (2012) describes additional data from the same

330 experiment that include (only for Case 1) current profiles measured below wave trough at 13

331 locations, as well as video imagery of the outer surf zone region near the reef crest recorded at 30

332 Hz. While the video images were not rigorously georeferenced, several horizontal and vertical

333 reference locations in the images were known, which allowed for a rough transformation of pixel to

334 world coordinates that enabled (at least a qualitative) comparison with the SPH simulations.

335   **2.4 Model application and numerical settings**

336   The numerical simulations were conducted using version 4.2 of DualSPHysics in a 2DV

337 (vertical) plane. To simulate the test cases, a numerical wave flume was constructed with a piston-

338 type wave maker located at the offshore boundary (Altomare et al., 2017), which included the exact

339 geometry of the beach in TK94 and reef in Y12. Both experiments were conducted in large wave

340 flumes that included a long uniform-depth region offshore of the beach / reef, thus creating a large

341 volume of water to resolve that greatly increased computational times, despite wave properties

342 being approximately constant across this offshore region. During initial model testing, we found

343 that reducing the length of this offshore regional had a negligible effect on the surf zone

344 hydrodynamics, so we shortened the offshore region by 10 m in the model applications of both

345 experiments.

346   For the TK94 spilling wave case, the offshore conditions with $H / gT^2 = 0.008$ and

347 $h / gT^2 = 0.03$ fell within the limits of second order wave theory, so second order wave generation

348 was used to drive the piston in DualSPHysics following Altomare et al. (2017). However, the

349 plunging wave case with $H / gT^2 = 0.0005$ and $h / gT^2 = 0.002$ fell within a cnoidal wave regime,

350 so the piston displacement timeseries was prescribed as model input based on cnoidal wavemaker

351 theory following Cho (2003). Both of the Y12 experiments had offshore wave conditions that fell

352   within the approximate limits of second order theory ($H / gT^2 = 0.006 - 0.010$ and

353    $h / gT^2 = 0.03 - 0.04$), which was used within DualSPHysics to drive the wavemaker.

354   To provide a rigorous and transparent assessment of model performance over the range of

355   test cases, we concentrated on using default or typical model parameter settings reported in the

356   literature that were held constant across all numerical results reported here, i.e. we did not vary

357   parameters across different test cases to optimize performance. However, during initial testing we

358   explored the model sensitivity to a subset of parameters (see Appendix A for details), focusing

359   specifically on the effect of: 1) initial inter-particle spacing (*dp*), 2) the artificial viscosity (α) and

360   3) the smoothing length (*h$_{SPH}$*) (see section 2.1).

361   Prior SPH studies of wave propagation have suggested that the initial inter-particle spacing

362   (*dp*) should be chosen to be at most 1/10 of the wave height or smaller to properly resolve the free

363   surface and hence minimize non-physical wave dissipation (e.g., Roselli et al., 2018). Therefore,

364   based on the incident wave heights (order 0.1 m across all test cases), this indicates that *dp* should

365   be 1 cm or smaller). From out testing, we found minimal improvement in model predictions of

366   wave height, setup and mean currents for *dp*<5 mm (see Appendix A and Supplementary Material);

367   however, for all simulations we conservatively used *dp*=2 mm. This translated to simulating ~1.22

368   million particles in both TK94 test cases, and ~1.24 million and ~830 thousand particles for Cases 1

369   and 3 of Y12, respectively.

370   The smoothing length *h$_{SPH}$* defines a length-scale that governs the size of the kernel that

371   determines particle-particle interactions in SPH (see section 2.1). In 2D, the smoothing length is

372   related to the initial inter-particle spacing according to $h_{SPH} = coefh\sqrt{2}dp$, where *coefh* is a

373   smoothing coefficient of order 1 that determines the scale of interactions with adjacent particles

374   (with typical values in the range of 1.2-1.8; Roselli et al. (2018)). With too low of value of *coefh*,

375   interactions of a given particle with its neighbouring particles diminishes, effectively leading to

376   numerical dissipation that can, for example, lead to some decay in waves propagating within

377   relatively large numerical wave flumes. Conversely, while increasing *coefh* can enhance energy

378   conservation, this increases the kernel size that effectively reduces model resolution by smoothing

379   the results over the length-scale *h$_{SPH}$*. For the present simulations, we found that values of *coefh*

380   between 1.0 – 1.8 had minimal effect on the results; however, wave height and mean current profile

381   predictions were slightly better for smaller values of *coefh* (see Appendix A and Supplementary

382   Material). Thus, in all simulations we used *coefh* = 1.2, which given *dp*=2 mm implies an effective

383   smoothing length of ~3 mm.

384   The SPH method requires some source of diffusion scheme to limit high frequency noise

385   and model instability. Various formulations have been proposed to introduce viscous dissipation in

386   the Lagrangian momentum equation, including sophisticated attempts to include turbulence closure

387   schemes (i.e., Sub-Particle turbulence models) that is analogous to a Large Eddy Simulation in

388   fixed-mesh models (e.g., Gotoh et al., 2004). Nevertheless, there still remain open questions on how

389   to best parameterize sub-particle scale turbulent motions in SPH (Violeau and Rogers, 2016), and

390   thus it is common to instead use an artificial viscosity (see Eq. (3)) that is designed to simulate a

391   minimal amount of viscosity to keep the numerical scheme stable. In this way, the artificial

392   viscosity coefficient (α) should be chosen to be small enough to allow turbulent motions of size

393   $>dp$ to be properly resolved, but large enough to avoid unstable solutions. A wide range of studies

394   have investigated the optimal value of α in numerical wave flume studies and have consistently

395   found this to be of order 0.01 (e.g., De Padova et al., 2014, Roselli et al., 2018, Altomare et al.,

396   2017, Roselli et al., 2019). Through a sensitivity analysis we found that model performance was not

397   significantly influenced by variations in α between 0.005 and 0.02 (see Appendix A and

398   Supplementary Material), and thus chose to use the default value $\alpha = 0.01$ recommended in

399   DualSPHysics within all runs.

400   **2.5 Numerical simulations and post-processing**

401   Under regular wave conditions, to attain quasi-steady state conditions that are required to be

402   able to resolve wave, mean current and turbulent properties, a number of studies (both experimental

403   and numerical) have found that of order 10 to 100 individual waves should be resolved (e.g., Ting

404   and Kirby, 1994, Jacobsen et al., 2012). For example, TK94 analysed the convergence

405   characteristics of the number (N) of waves averaged to accurately resolve both mean currents and

406   turbulence statistics, and found this occurred after roughly $N=40$ wave periods. We thus

407   conservatively ran the SPH simulations for 360 seconds, which corresponded to resolving $N=180$

408   waves and $N=72$ waves for the TK94 spilling and plunging cases respectively, and $N \approx 300$ waves

409   for the Y12 test cases. Raw properties (e.g., velocities, pressure, etc.) of the field of particles

410   simulated by DualSPHysics were output at 50 Hz.

411   All numerical simulations were conducted at the Pawsey Supercomputing Centre in Perth,

412   Australia on a supercomputer (Zeus) with GPU-capable nodes. Each compute node on Zeus

413   contains four Intel Xeon E5-2680 v4 2.4GHz (14 core, 28 thread), each with 256 GB RAM and a

414   dedicated Nvidia Tesla P100 GPU (i.e., 4 GPUs per node). As multi-GPU functionality is not

415   currently available in DualSPHysics, to optimise model performance we packed 4 simulations at a

416   time onto each node of Zeus. Under this configuration, the simulation of all four test cases for 360

417 seconds (real world time) took approximately 63 hr for both the TK94 spilling and plunging cases;

418 and 67 hr and 45 hr for Case 1 and 3 in Y12, respectively.

419   To compare the simulation results to the fixed (Eulerian) experimental measurements, for an

420 array of points specified on a grid, a Wendland kernel function (averaging length $2h_{SPH}$) was used to

421 interpolate the individual SPH particle properties to the grid (Wendland, 1995). The resolution of

422 the postprocessing grid varied to coincide with instrument measurement locations and/or to

423 investigate specific process-questions using the numerical output. However, to specifically detect

424 free surface positions across flumes to compare with wave height observations, postprocessing with

425 a much finer vertical grid resolution $\Delta z = 1$ mm was used. The vertical free surface positions were

426 detected as the elevation where the averaging kernel was 40% water by mass (a recommended

427 threshold in 2D versus 50% in 3D), which was obtained by identifying the first point that satisfied

428 this criterion when searching upwards in the water column from the bottom. We note that for the

429 case of plunging waves where the free surface overturns, there can be multiple definitions in the

430 specification of a (single valued) "free surface" height (e.g. alternatively the maximum free surface

431 point could be chosen). However, when comparing the results to experimental measurements, it is

432 equally unclear which water level a capacitance / resistance wire wave gauge would precisely

433 record when there is a mixture of water and air along the gauge. Therefore, we chose to adopt the

434 present approach (a common approach incorporated in DualSPHysics), while acknowledging that

435 some discrepancies between the experimental data and model results could be expected within the

436 surf zone of the plunging wave cases.

437   The raw timeseries of a given property (e.g., velocities, water levels, etc.) were then

438 decomposed into mean and wave (and in the case of velocities, turbulent) contributions by

439 ensemble averaging over the periodic waves (e.g., Nielsen, 1992). Thus, for example, for the

440 horizontal velocity component (u), this was decomposed as (e.g., Nadaoka et al., 1989)

441
$$u(t) = \overline{u} + \tilde{u}(t) + u'(t) \qquad (8)$$

442 where the overbar (–) denotes averaging over a timescale much greater than the wave period, the

443 tilde (~) denotes the wave (periodic) contribution, and the prime (') denotes the turbulent

444 ("random") contribution. The wave velocities ($\tilde{u}$) were obtained by subtracting the mean current

445 velocity ($\overline{u}$) from the ensemble-averaged velocities,

446
$$\tilde{u}_i = \frac{1}{N} \sum_{j=1}^{N} u_{i,j} - \overline{u} \qquad (9)$$

447   where *i* represents a time (wave phase) counter, *j* a wave series counter and *N* represents the number

448   of waves averaged over. Turbulent velocities are then defined based on removing the mean current

449   and wave contributions from the raw velocity timeseries, $u' = u - \overline{u} - \tilde{u}$.

450   We note that in the WCSPH approach, density (pressure) fluctuations can introduce some

451   degree of noise that can translate into velocities. To understand the magnitude of this possible noise

452   relative to the turbulent velocities within the surf zone, we conducted a reference simulation with

453   still water (i.e. no wavemaker motion) using the identical geometry, model configuration, and

454   simulation duration that was used in the TK94 runs. Such an approach is analogous to the WCSPH

455   study by Wei et al. (2018), who assessed the background kinetic energy in a still wave flume to

456   investigate the role that small velocity perturbations may play in the chaotic breaking behaviour of

457   waves. For the still water case, we found that the background kinetic energy density was very small

458   (on-average of order 10^{-9} m^2 s^{-1}, not shown), which was approximately six orders of magnitude

459   smaller than typical turbulent kinetic energy densities of order 10^{-3} m^2 s^{-1} that were predicted within

460   the surf zone (see below). As a consequence, any numerical noise associated with the WCSPH

461   scheme should be negligible relative to the range of turbulent hydrodynamic motions simulated in

462   this study.

463   Finally, in a similar way to velocity, the timeseries of water elevation (η) relative to still

464   water level were decomposed into a time-averaged mean water level ($\overline{\eta}$) (i.e., a wave setup

465   contribution) as well as a periodic, phase-dependent wave contribution ($\tilde{\eta}$) by ensemble averaging

466   over the *N* waves. To quantify the cross-shore evolution in the nonlinearity of wave shape, both the

467   skewness (*Sk*) and asymmetry (*As*) were calculated from $\tilde{\eta}$ as (e.g., Ruessink et al., 2012):

468
$$Sk = \frac{\overline{\tilde{\eta}^3}}{\left(\overline{\tilde{\eta}^2}\right)^{3/2}}, \quad As = \frac{\overline{\tilde{\eta}_H^3}}{\left(\overline{\tilde{\eta}^2}\right)^{3/2}} \tag{10}$$

469   where for *As* the subscript *H* denotes the Hilbert transform of $\tilde{\eta}$. The skewness describes how the

470   crest is much more elevated and narrower to the trough; whereas the asymmetry describes how

471   pitched forward/backward (i.e., "saw-toothed") the waves are.

472

473   **3   Results**

474   **3.1 Wave breaking over a plane beach (Ting and Kirby, 1994)**

475   Although both of the TK94 test cases had breaking wave heights that were approximately

476   the same, the difference in wave period resulted in appreciable differences in how waves broke and

477   transformed within the surf zone (Figure 2). For the "spilling" case, the model predicts a slight

16

478   overturning of the free surface (albeit a small volume of water) that initiates at a breaking location

479    $x_b \approx 6.5$ m, which evolves into a turbulent bore that propagates shoreward. For the "plunging" case,

480   the waves undergo greater shoaling, the break point is located further inshore ($x_b \approx 7.5$ m) and there

481   is a much larger overturning (hollow) region during breaking. The initial plunging jet then triggers a

482   sequence of splash-up events from the free surface that propagate well into the inner surf zone.

483   For both test cases, the cross-shore variations in wave heights are accurately predicted, as

484   illustrated here by comparison of the ensemble-averaged crest (η_{max}) and trough locations (η_{min})

485   (Figure 3a,b). Small discrepancies tend to fall within the variability among individual waves, and

486   possibly well-within the uncertainty of the measurements using capacitance wire wave gauges in

487   the aerated surf zone region, which TK94 note may lead to errors that are difficult to quantify. The

488   cross-shore variations in wave setup ($\overline{\eta}$) are also well-predicted by the model (Figure 3c,d). For the

489   spilling case (Figure 3c) there is an abrupt jump in setup at $x \approx 5.5$ m immediately seaward of the

490   breakpoint that is not consistent with the gradual increase in setup through the surf zone that is

491   predicted with the model. As noted in a number of other studies using this TK94 case (e.g.,

492   Cienfuegos et al., 2010, Tonelli and Petti, 2010, Smit et al., 2013), a physical explanation for this

493   small jump in setup is unclear and potentially could reflect some measurement artefact for the wave

494   gauge(s) near the breakpoint.

495   Figure 4 shows the wave water level timeseries ($\tilde{\eta}$), which are ensemble-averaged over a

496   wave period, as well as the skewness (*Sk*) and asymmetry (*As*) parameters that characterize

497   nonlinear wave shape (Eq. (10)). For the four example locations shown, which span the shoaling,

498   outer surf zone, and inner surf zone regions, the $\tilde{\eta}(t)$ timeseries agree well with the observations.

499   This includes reproducing the more complex wave shapes for the plunging case, where there is very

500   rapid rise of the free surface just prior to the arrival of the crest, followed by the much slower fall of

501   the free surface that includes an inflection (small second local maximum) in the water level. While

502   this inflection is slightly more pronounced in the observations, its occurrence and timing are still

503   predicted by the model. The close agreement between the modelled and observed wave skewness

504   and asymmetry is particularly remarkable, given this covers a large number of measurement

505   locations and wave states as they transform from deep water to the shoreline, and given that as

506   third-order bulk statistical parameters of the waves are generally more difficult to predict relative to

507   wave heights. For the spilling case, the model captures the significant increase in *Sk* as the waves

508   steepen in the shoaling zone up the breakpoint ($x_b \approx 6.5$ m), which is followed by a gradual return

509   towards a linear wave shape as the shoreline is approached (Figure 4e). Similarly, the model

510   captures the two inflections (local maxima) in *As* that are observed seaward of the breakpoint and

511   the sharper decrease in As (more negative, implying a pitched forward wave face) that occurs

512   shoreward of the breakpoint. While the available data for the plunging case are more limited, which

513   only include measurements shoreward of the breakpoint, the modelled Sk and As agree similarly

514   well with the observations.

515   The mean Eulerian current profiles show distinct reversals in flow above and below the

516   mean wave trough elevation consistent with an expected undertow profile, with onshore flow within

517   the crest region and offshore flow below the trough (Figure 5). As noted by TK94, due to

518   restrictions with the LDA measurements they were only able to obtain a small portion of valid data

519   above the trough; however, they measured the entire water column beneath it. The modelled mean

520   current profiles are generally in good agreement with the observations. Above the trough, the model

521   compares reasonably well in the lower portion of the region where measurements could be made;

522   further above this elevation (where no observations are available), the model predicts a local

523   maximum in each current profile with the velocity then decreasing again towards the crest. Below

524   the trough, for the spilling case the model tends to accurately predict the shape and magnitude of the

525   undertow profile; however, at some locations shoreward of the breakpoint (particularly those at

526   x=7.0-8.5 m), the model tends to predict a slightly more vertically-sheared profile. For the plunging

527   case, the undertow within the inner surf zone (x>8.5 m) is also accurately predicted; however,

528   similar to the spilling case, within the outer surf zone immediately seaward of the breakpoint (i.e.,

529   locations x=7.0 – 8.5 m), there is marginally more vertical shear in the undertow profile than

530   observed and overall there is slightly too much flow offshore.

531   **3.2 Wave breaking over a fringing reef (Yao et al. 2012)**

532   The two Y12 cases have similar offshore wave conditions but use different offshore still

533   water levels (Figure 6). In both cases, strong plunging waves break over the steep forereef slope;

534   however, the difference in still water level greatly influences how rapidly the waves break and

535   dissipate energy within the surf zone. For Case 1, where the still water depth over the reef is h_r=0.1

536   m, wave breaking occurs near the crest (x=0 m), and after a sequence of splash-up events, a bore

537   propagates shoreward that allows wave energy to be transmitted across the reef flat. For Case 3, the

538   still water depth over the reef is h_r=0.0 m; however, due to wave setup, there is still on average a

539   small depth of water over the reef flat (~0.04 m). Due to the shallow depth, for this case the wave

540   drawdown preceding breaking causes the forereef slope to be nearly dry (minimum ensemble-

541   averaged depth of ~2 cm), causing the plunging jet to impinge on the bottom, leading to a large

542   splash-up of water. Nearly all of the incident wave energy is dissipated near the crest region, with

543   the presence of only a small depth-limited bore propagating across the reef flat.

18

544   Y12 recorded video imagery of the surf zone region for Case 1, and while the imagery is not

545   rigorously georeferenced and there can be variability between individual breaking waves, it can at

546   least be qualitatively compared to the free surface profiles predicted by the model. Figure 7 shows

547   an image sequence of an individual breaking wave with the free surface predicted by the model

548   superimposed. Note that even with regular wave breaking there is some expected variability in how

549   individual waves break (i.e., due to some element of chaotic behaviour as described by e.g. Wei et

550   al. (2018)) and the video was not synchronized with the wavemaker or instrumentation. Therefore,

551   in Figure 7 we compare the breaking of an arbitrary wave, which tends to reproduce the main

552   features of the breaking process well, including the initial plunging wave shape, an initial splash-up,

553   and subsequent propagation of the bore across the reef flat.

554   The model accurately predicts the ensemble-averaged wave crest ($\tilde{\eta}_{max}$) and trough ($\tilde{\eta}_{min}$)

555   elevations for both cases (Figure 8). The wave setup ($\bar{\eta}$) profiles are also reproduced reasonably

556   well, with good agreement with the maximum setup generated over the reef flat, including the much

557   greater setup (factor of ~3) for the shallower depth Case 3. For Case 1, the model predicts less

558   setdown in the shoaling zone near the crest (Figure 8c), and for Case 3, does not predict the jump in

559   wave setup further back on the reef flat at $x \approx 1.7$ m (Figure 8d). For Case 3, this significant jump

560   in setup (~20%) would likely to be an experimental artefact, as there is effectively no wave energy

561   remaining at this location on the reef (and hence no radiation stress gradients) to explain a sudden

562   generation of wave setup. For Case 1, the cause of the discrepancy in setdown is not clear, although

563   we note that Y12 found that setdown was similarly underpredicted using a Boussinesq wave model

564   simulation applied to this same case.

565   The model predictions of wave shape generally agree well with the observations, as

566   illustrated by the comparison of the ensemble-averaged water level timeseries at four locations, as

567   well as the agreement with the skewness and asymmetry properties over the whole domain (Figure

568   9). For Case 1, the predicted water level timeseries are nearly in exact agreement with the

569   observations (Figure 9a-d). For Case 3, the predicted water level timeseries agree well at locations

570   offshore of the crest (x<0) (Figure 9g-i); however, there is slightly poorer agreement on the reef flat,

571   albeit at this location the wave heights are minimal ($H \approx 0.006$ m), and hence more than an order of

572   magnitude smaller than offshore. For Case 1, the skewness (*Sk*) and asymmetry (*As*) patterns across

573   the reef profile are rather striking, with a series of oscillations that are present in both the

574   observations and model predictions. For Case 3, there is poorer agreement between the model

575   predictions and observations, particularly over the reef flat (x>0 m); however, the wave heights over

19

576 the reef flat are very small (order 1 mm) and thus would exaggerate any small differences between
577 the model and observations.

578   To understand the causes of the oscillations in wave skewness and asymmetry across the
579 reef flat, we further investigate how individual waves change in shape as they propagate shoreward
580 from the surf zone (Figure 10). Eldeberky and Battjes (1995) observed analogous reversals in the
581 skewness and asymmetry of waves during experiments investigating how waves transform as they
582 propagate across a trapezoidal bar, which they attributed to the release of bound super-harmonic
583 waves that, once free, move with different phase speeds and then alter wave shape as they interact.
584 The wave spectrum at the seaward portion of the reef flat (x=2 m) shows that there is significant
585 wave energy in the first two super-harmonics (f_1 and f_2) (Figure 10a), which as free waves with
586 different frequency f would propagate at different speeds $c(f)$, even in the shallow water depth over
587 the reef flat. This is illustrated in Figure 10b, where the wave propagation pathlines $x(t) = c(f)t$
588 based on linear wave theory predict that both f_1 and f_2 move slower than a wave with the incident
589 fundamental frequency (f_0). Evidence for the release of super-harmonics is particularly clear for f_2
590 in Figure 10b, where a distinct separate wave crest moves at the phase speed predicted by the
591 second harmonic. Initially this wave contributes to steepening the front face of the wave (hence
592 negative As) but once it interacts with the next wave of frequency f_0 shoreward on the reef flat it
593 generates a steeper back face (hence positive As). This swap in wave shape is also clearly visible in
594 the ensemble-averaged water level profile across the reef flat shown in Figure 10c.

595   Y12 only conducted mean current profile measurements for Case 1, which were obtained
596 only below the wave trough level (Figure 11). The model generally reproduces the main features of
597 the mean current profiles across the reef reasonably well. An interesting feature of the current
598 profiles is the reversal of the undertow profile below the trough that occurs on either side of the reef
599 crest (i.e., increasing towards the bottom shoreward of the reef crest; decreasing towards bottom
600 seaward of the reef crest), which is reproduced by the model.

601

602 **4   Discussion**

603   **4.1 Wave transformation and wave setup**

604   The cross-shore variations of wave heights and wave shape were accurately reproduced by
605 the SPH simulations over the range of different wave conditions and bathymetry profiles that were
606 considered in this study. This included a broad range of different wave breaking types, spanning the
607 extremes of spilling waves breaking on a plane beach in TK94 (Figure 3) to the strongly plunging
608 waves breaking on a nearly dry, steep reef slope in Y12 (Figure 8). The excellent agreement with

the cross-shore evolution of individual wave shape was particularly notable, given how the test
cases included complicated and variable changes in the skewness and asymmetry properties of the
waves as they propagated across the bathymetry profiles (Figure 4, Figure 9). For example, this was
illustrated by the accurate reproduction of the complex skewness and asymmetry oscillations across
the reef profile in Y12 (Figure 9), which was achieved by correctly resolving the release of super-
harmonics within the surf zone that then disperse with different celerities across the reef platform
(Figure 10). Perhaps most significant overall, the SPH simulations were able to reproduce the
complex wave transformation processes using a fixed set of numerical parameters using
recommended / default values, which required no tuning among the different cases despite the very
different wave breaking characteristics.

Nevertheless, it is also important to acknowledge that other phase-resolving modelling
approaches based on fixed meshes have also been successful in reproducing wave transformation
over a similar range of wave breaking extremes (including for the same case studies considered
here); however, these models often require tuning of empirical parameters that can reduce their
general predictive skill. As (quasi) depth-averaged versions of these models (e.g., based on
Boussinesq and non-hydrostatic approaches) cannot resolve the overturning of the free surface and
details of wave breaking, they require some parameterization to describe the breaking process. For
example, within Boussinesq models this has commonly been based on the inclusion of empirical
roller models (e.g., Schäffer et al., 1993, Madsen et al., 1997) or eddy viscosity formulations (e.g.,
Cienfuegos et al., 2010, Kennedy et al., 2000); whereas, non-hydrostatic models have tended to use
momentum-conserving shock-capturing schemes that treat wave breaking similar to a hydraulic
jump (e.g., Zijlema et al., 2011, Ma et al., 2012). For depth-averaged (i.e., single layer) and coarse
multi-layer (less than about ten vertical layers) non-hydrostatic models, the acceleration of the crest
region that triggers breaking and subsequent development of saw-tooth bores cannot be accurately
captured; so these models often use a "hydrostatic front approximation" (HFA) when a critical wave
steepness locally occurs that quickly transitions the surface into a bore-like shape that dissipates
energy (Smit et al., 2013). Despite the relative simplicity of how the wave breaking physics within
(quasi) depth-averaged models are described, they have nonetheless been able to reproduce many of
the characteristics of wave transformation, including for model applications to the same test cases,
i.e., for both TK94 (Roeber et al., 2010, Bredmose et al., 2004, Lynett, 2006, Tissier et al., 2012,
Cienfuegos et al., 2010, Derakhti et al., 2016a, Bradford, 2010) and Y12 (e.g., Yao et al., 2012,
Zhang et al., 2018b). However, to achieve this requires adjusting empirical parameters that affect
wave energy dissipation within these models (including the onset and cessation of breaking) (e.g.,

642 Smit et al., 2014), which can vary for different breaking wave conditions and hence does not strictly

643 have a strong physical basis.

644   Three-dimensional (3D) phase-resolving wave-flow models that resolve the vertical

645 structure, on the other hand, can provide a more complete description of the wave breaking process.

646 For the case of CFD models based on RANS or LES (for example, applications of OpenFOAM),

647 they are able to simulate overturning breaking waves on a fixed mesh, including surf zone

648 turbulence. While computationally expensive, these approaches have been very successful in

649 reproducing a wide range of nearshore hydrodynamic processes observed in experimental studies.

650 For example, a number of studies have similarly compared CFD models to the experimental

651 observations of TK94, and found that these approaches can accurately reproduce surf zone wave

652 transformation and wave setup profiles with comparable skill to the present study (e.g., Jacobsen et

653 al., 2012, Brown et al., 2016, Larsen and Fuhrman, 2018). Notably, these studies have suggested

654 that predictions of wave transformation and setup profiles are not particularly sensitive to having

655 very accurate reproduction of the surf zone turbulence. For example, Brown et al. (2016) assessed 6

656 turbulence closure schemes and found that all could reproduce the surface elevations observed in

657 TK94 (see Figure 2 in that paper), despite the significant differences in the mean and turbulent flow

658 structures predicted by these approaches (see further discussion below).

659   Multi-layered nonhydrostatic models such as SWASH (Zijlema et al., 2011) and NHWAVE

660 (Ma et al., 2012) were developed to be more computationally efficient alternatives to CFD models,

661 albeit they describe the free-surface with a single value and thus do not attempt to reproduce the

662 overturning that occurs during breaking. Nevertheless, despite this rather crude representation of the

663 breaking physics, with sufficient vertical resolution, these models have proven to be remarkably

664 robust at reproducing wave transformation and setup profiles over a wide range of wave conditions

665 (including plunging), without the need for use of the HFA to trigger the onset of breaking (and

666 hence avoiding the need to specify an empirical parameter to prescribe the maximum wave

667 steepness). For example, Smit et al. (2013) investigated how multi-layered applications of SWASH

668 performed at simulating the TK94 experiments with the HFA disabled. They found that with 20

669 layers the initiation of breaking could be accurately captured even for plunging waves, resulting in

670 robust predictions of both the wave transformation and setup distributions, independent of a detailed

671 resolution of the breaking process.

672   Overall, it appears that for nearshore applications where the primary aim is to accurately

673 predict the water level variations through the surf zone (not necessarily details of the mean and

674 turbulent flow structure), the use of a nonlinear phase-resolving model is of utmost importance.

675 However, models with finer vertical resolution (i.e., 3D or 2DV) are required to capture wave

676   breaking without calibration, as depth-averaged or coarse vertical resolution Boussinesq-type and

677   non-hydrostatic models rely on some sort of breaker model (that either accounts for the dissipation,

678   such as the eddy viscosity and roller approach, or triggers the initiation of wave breaking, such as

679   the HFA approach). Therefore, the results suggest that both mesh-based (i.e., CFD, non-hydrostatic

680   and Boussinesq-type) and mesh-free (i.e., SPH) models can all be equally capable of delivering

681   accurate predictions of wave transformation and setup despite differences in how they reproduce the

682   detailed characteristics of breaking waves.

4.2 Wave-driven transport and surf zone turbulence

684   The SPH simulations provided reasonably accurate representations of the cross-shore

685   variations in the mean flow structure observed within both the TK94 (plane beach) and Y12 (reef

686   profile) experiments. For the TK94 experiments, the magnitude of the undertow strength was

687   generally well predicted, albeit with some discrepancies observed in the vertical flow profiles at

688   some cross-shore locations. For both the spilling and plunging cases (Figure 5), the model results

689   displayed some remarkable agreement with the observations, particularly within the inner surf zone

690   ($x > 8.5$ m); there were only some small discrepancies observed in the outer surf zone immediately

691   near or shoreward of the breakpoint (7.0 m $< x <$ 8.5 m) where the modelled profiles were slightly

692   more sheared. For the available flow measurements above the mean wave trough elevation, the

693   simulations accurately reproduced the onshore mean transport profile within the crest region (Figure

694   5) and given the good agreement with offshore volume flux below the trough, an equally good

695   agreement with the onshore volume flux within the crest region that could not be measured can also

696   be inferred.

697   Given that the accurate prediction of cross-shore transport in the nearshore is critical to a

698   wide range of applications (e.g., understanding how waves drive beach erosion and recovery

699   cycles), several studies have investigated the performance of numerical models to reproduce

700   experimental observations of wave-driven mean flows. These studies include those using 3D / 2DV

701   phase-resolving wave-flow models solved on fixed grids using the same TK94 experiments to

702   benchmark model performance, which can therefore provide valuable context to the present SPH

703   results. Rijnsdorp et al. (2017) and Derakhti et al. (2016a) applied the multi-layered non-hydrostatic

704   model approach to evaluate its ability to reproduce the mean current profiles observed in TK94 (see

705   Figure 6 in the first, and Figure 3 and 4 in the latter study). While both studies found that the non-

706   hydrostatic approach could reproduce the main features of the current profiles reasonably well, the

707   results deviated significantly more than in the present study, with both an overprediction of the

708   onshore transport in the crest region (by a factor of 2 for the plunging case) and with a similar

23

709   overprediction of the offshore undertow transport (i.e., defined by more exaggerated belly-shaped

710   profiles). Several studies have also applied CFD models (i.e., OpenFOAM) to the TK94

711   experiments, and have often also observed a significant overprediction of the undertow transport

712   compared to the present SPH results, particularly when using conventional RANS-based turbulence

713   closure models (e.g., Jacobsen et al., 2012, Brown et al., 2016, Larsen and Fuhrman, 2018,

714   Devolder et al., 2018). Brown et al. (2016) were able to improve predictions of the undertow

715   profiles by adopting more sophisticated turbulence closure schemes (for example, see Figures 5 and

716   8 in Brown et al. (2016) for comparisons with the spilling and plunging cases, respectively);

717   however, in all cases the model overpredicted the undertow velocities more than in the present

718   study, especially within the inner surf zone region where agreement with the SPH results were

719   excellent. Larsen and Fuhrman (2018) observed similar overpredictions of the undertow in their

720   CFD simulations, which they believed was due to surface rollers travelling too fast due to local

721   underpredictions of eddy viscosities (hence flow resistance) simulated within the upper-most part of

722   the water column, leading to increased onshore flows above the wave trough and increased return

723   flows below the wave trough. While the undertow profiles were generally accurately predicted

724   using the present SPH approach, the small discrepancies observed could likewise be due to some

725   deviations in the vertical turbulent flow structure predicted within the inner surf zone.

726   The ability of the present SPH simulations to more accurately predict the mean current

727   profiles in TK94 relative to a number of CFD model applications is somewhat surprising, given that

728   no sub-particle scale turbulence closure model was used; albeit, the simulations themselves were

729   conducted at relatively fine resolution (order 1 mm) where at least many of the larger-scale wave-

730   generated turbulence would be expected to be resolved. However, before discussing the role of

731   turbulence on the current profiles, it should be first acknowledged that some of the improved

732   performance of the SPH results over many prior CFD studies could be due to a more robust

733   representation of the onshore mass transport within the crest region of the breaking waves, which

734   was overpredicted in all of the aforementioned studies (in contrast to present SPH simulations

735   where there was generally excellent agreement). Given that any overprediction of onshore mass

736   transport would lead to an overprediction of the undertow transport below the trough, independent

737   of how vertically distributes the momentum, at least some of the strong performance of the SPH

738   simulations could simply be better resolution of the onshore mass flux in the crest region during

739   breaking. This might be expected when comparing to the case of a non-hydrostatic model where a

740   single-valued representation of the free surface cannot truly resolve overturning wave breaking,

741   potentially leading to some discrepancy in onshore mass flux. However, CFD models based on

742   VOF are arguably able to resolve the overturning free surface, albeit at a resolution prescribed by

743   the numerical mesh (ranging from 0.005 – 0.01 m in the aforementioned studies). Further work is

744   required to understand the capabilities and limitations of different modelling approaches (both

745   fixed-mesh and mesh-free) to accurately predict mass transport within the crest region of breaking

746   waves; this would also be best investigated using additional experimental datasets with more

747   observations than TK94, which only reported observations within the lower portion of the wave

748   crest.

749   Once a model simulates a given onshore mass flux within the wave crest, the properties of

750   the surf zone turbulence then influence the vertical distribution of the undertow profile. Given that

751   surf zone turbulence spans a broad range of scales, the SPH simulations would include motions that

752   are directly resolved (i.e., at scales greater than the averaging kernel) but would neglect smaller

753   (sub-particle) scale that would only be parameterised using a simple viscosity formulation in the

754   present study. As defined in Eq. (8), for regular waves it is conventional to decompose an

755   instantaneous velocity timeseries $u(t)$ via ensemble averaging into a mean ($\bar{u}$), wave ($\tilde{u}(t)$), and

756   turbulent ($u'(t)$) motions; in this sense, turbulence is defined as any unsteady motions that are non-

757   periodic (Nadaoka et al., 1989). While a detailed investigation of the surf zone turbulence predicted

758   by the SPH simulations is beyond the scope of the present study, and would also be best

759   complemented by detailed assessments of sub-particle scale (SPS) turbulence closure models that

760   have been implemented in SPH, it is nonetheless interesting to assess what the present high-

761   resolution model simulations predict using the turbulent motions that are directly resolved within

762   the resolution of the simulations. Figure 12 compares the mean turbulent kinetic energy (TKE) $\bar{k}_t$

763   reported in TK94 for the spilling and plunging cases with the model predictions. Note that for

764   comparison we adopt the identical analysis approach presented in TK94, where given that

765   transverse flows were not measured (and also not simulated in the 2DV simulations), the wave

766   phase-varying TKE was calculated as $k_t = \left(1.33/2\right)\left(\overline{u'^2} + \overline{w'^2}\right)$ and then time-averaged to obtain $\bar{k}_t$.

767   For both the spilling and plunging cases, the model agrees reasonably well with the observations

768   within the inner surf zone region (i.e., $x>9$ m and 10 m for the spilling and plunging cases,

769   respectively); however, within the outer surf zone towards the break point, the model overpredicts

770   the mean TKE. A number of CFD and non-hydrostatic model applications of TK94 have also

771   compared TKE predictions (e.g., Jacobsen, 2011, Larsen and Fuhrman, 2018, Rijnsdorp et al., 2017,

772   Brown et al., 2016), and have similarly found TKE to be significantly overpredicted when using

773   conventional turbulence closure schemes within RANS-based models. This has motivated the

774   application of more sophisticated closure models (e.g., Devolder et al., 2017, Brown et al., 2016)

775   that consider, for example, the stabilizing effects of buoyancy due to entrained air, which has helped

776 to improve model agreement; nevertheless, it is still widely recognized that there is considerable

777 scope to further improve parameterization of sub-grid scale turbulence within surf zone applications

778 within these models.

779   For the present SPH simulations, it is interesting that the computed TKE was overpredicted

780 even with no turbulence closure (i.e., SPS) model included. Within SPH, turbulent motions can, in

781 general, be described as those that can be directly resolved at the particle resolution (i.e., $>h_{SPH}$) and

782 those sub-particle scale motions that may be parameterized within a turbulence model (if included

783 within an application) (e.g., Dalrymple and Rogers, 2006). Therefore, analogous to how turbulence

784 is described in fixed-grid CFD models (i.e., either RANS or LES), where the TKE should be a

785 superposition of the turbulent motions resolved on the grid and the sub-grid scale turbulence

786 parameterized by the closure model, the inclusion of an SPS closure model in the present study

787 would potentially result in an even greater over prediction of the total TKE. While the source(s) of

788 the overprediction of TKE in the present SPH simulation are unclear, and may be due to both the

789 two-dimensional nature of the simulations and the simplified treatment of viscous stresses in the

790 present study, at least another potential candidate could include the absence of multi-phase

791 behaviour within the simulations, where in reality the buoyancy of entrained air during breaking

792 would be expected to have some stabilizing effect on any turbulence generated, which has been

793 identified in various CFD studies of surf zone turbulence (e.g., Devolder et al., 2018).

794   Given that the model appears to resolve a significant amount of turbulence generated within

795 the surf zone, we can also assess how the spectral properties of the turbulent velocity fluctuations

796 compare with known trends reported in the literature. Figure 13 shows power spectra for both

797 horizontal ($S_{u'u'}$) and vertical ($S_{w'w'}$) turbulent velocity components at two locations (outer and

798 inner surf zone) and at two elevations (mean trough elevation and near the bottom) for the spilling

799 case. Within these figures, there are regions where the spectra display both -3 and -5/3 slopes (in

800 log-log space) that are commonly observed within surf zone turbulence measurements. Within the

801 outer surf zone where incipient breaking occurs (x=7 m), at the mean trough elevation there is a

802 well-defined -3 slope for f >1 Hz (Figure 13a). Near the bottom (Figure 13b), there is also a -3 slope

803 between $1 < f < 5$ Hz; however, at higher frequencies ($f > 5$ Hz) a -5/3 slope is observed. Within the

804 inner surf zone (x=10 m), at the mean trough elevation there is also a broad region ($f > 3$ Hz) with a

805 -3 slope (Figure 13c). Near the bottom, the horizontal velocity spectrum ($S_{u'u'}$) displays both -3 and

806 -5/3 sloping regions (Figure 13d); however, the vertical velocity spectrum ($S_{w'w'}$) displays a -5/3

807 slope over a broad range ($f > 0.5$ Hz).

808   A number of experimental studies have investigated the spectral properties of surf zone

809   turbulence, which have frequently found that the spectral shapes are initially dominated by a -3

810   slope close to the breaking point (both in cross-shore location and towards the free surface), which

811   transitions to increasingly -5/3 slopes as the wave breaking evolves shoreward (e.g., Stansby and

812   Feng, 2005, Lakehal and Liovic, 2011, Hattori and Aono, 1985, Lemmin et al., 1974, Battjes and

813   Sakai, 1981). Ting and Kirby (1996) report the turbulent velocity spectra for the TK94 spilling case,

814   albeit at only one cross-shore location within the inner surf zone (x=10.4 m) and within the lower

815   portion of the water column (both near the bottom and at intermediate depth between the trough and

816   bottom), where a dominant -5/3 spectral slope was observed for $f > 1$ Hz. This location is most

817   closely related to the model results presented in Figure 13d, where the vertical turbulent velocity

818   spectrum ($S_{w'w'}$) also displays a broad -5/3 slope for $f > 1$ Hz; however, for the horizontal

819   component ($S_{u'u'}$) the model predicts a narrower -5/3 region confined to higher frequencies ($f > 4$

820   Hz), with a steeper -3 slope observed at intermediate frequencies ($1 < f > 4$ Hz). While the cause of

821   this discrepancy is not entirely clear, this would likely be due to the 2D representation of turbulent

822   motions in the present simulations that would likely not adequately describe the turbulent energy

823   cascade that would be present within experiments. For example, based on theory of 2D

824   homogeneous turbulence, an inertial sub-range with a -5/3 spectral slope is predicted to occur at

825   small spatial-scales, thus similar to the inertial sub-range for 3D turbulence (Lesieur, 2008).

826   However, for 2D the direction of energy flow within this inertial sub-range can be from small to

827   large scales, thus opposite to the direction with 3D turbulence. A detailed investigation of surf zone

828   turbulence, including the role of 2D versus 3D turbulent motions, is well beyond the scope of the

829   present study but should be conducted in the future. However, given that the present 2D model

830   results are qualitatively consistent with trends in experimental observations of surf zone turbulence,

831   this suggest that at least some of the important turbulent motions can be resolved by 2D

832   simulations.

833   **4.3 Implications for improved understanding and predictions of surf zone processes**

834   Overall, the results indicate that the SPH approach can be used as a robust and powerful tool

835   to simulate detailed surf zone hydrodynamic processes, with comparable model skill to state-of-the-

836   art mesh-based CFD models. This conclusion is analogous to recent work by González-Cao et al.

837   (2019) who evaluated the ability of both a mesh-free (DualSPHysics) and mesh-based

838   (OpenFOAM) CFD models to simulate wave impacts on coastal structures, and found that both

839   models reproduced the experimental observations with similar accuracy.

840   One potential strength of SPH models is their inherent suitability for simulating wave

841   breaking (including overturning plunging waves) where the free surface displacements are

842   extremely variable, and hence do not naturally conform to a fixed mesh. The results suggest that a

843   mesh-free SPH approach can provide robust predictions of surf zone wave breaking and help to

844   overcome some of the inherent challenges with quantifying hydrodynamic processes near the free

845   surface (in particular within the critical crest-to-trough region) that are extremely difficult to

846   measure experimentally. On this basis, further analysis of the SPH model results should help to

847   provide new insight into surf zone processes (including momentum and energy balances) beyond

848   conventional phase-resolving wave models. Therefore, while a comprehensive investigation of

849   these surf zone processes is beyond the scope of the present study, here we highlight some

850   additional aspects of the results that are particularly relevant to understanding wave transformation

851   and momentum balances in the nearshore.

852   As an example, we can further examine the results for the spilling case of TK94, where a

853   region of elevated positive (clockwise) vorticity emerges within the crest region as each wave

854   breaks (Figure 14). This concentrated region of vorticity coincides with formation of a roller

855   (Svendsen, 1984), where potential energy within the wave is initially converted to organized kinetic

856   energy, prior to dissipation occurring. As the roller propagates shoreward within the wave crest, it

857   leaves behind a series of surf zone eddies (rotating both clockwise and counter-clockwise). Pairs of

858   eddies with counter-rotating vorticity appear to cause water within the crest to be advected

859   downwards towards the seabed (i.e., sequence from Figure 14c to d), analogous to the descending

860   eddy pairs that have been observed in detailed experimental and numerical studies of breaking

861   waves (e.g., Nadaoka et al., 1989, Farahani and Dalrymple, 2014, Zhou et al., 2014). These eddies

862   also persist to some degree over a full wave cycle, with a following wave interacting with residual

863   eddies that were previously generated during breaking (i.e., Figure 14a).

864   The spatial variability in the water levels and flows (mean and turbulent) generated during

865   breaking ultimately determine the mean (wave-averaged) momentum balances that govern wave

866   setup distributions and mean currents through a surf zone. Given that the SPH approach should

867   resolve additional physics relative to conventional phase-averaged and phase-resolving wave

868   models, we can further interrogate the results to examine how various processes that are generally

869   neglected (or parameterized) in conventional models influence wave transformation, and in turn

870   how they influence predictions of cross-shore momentum balances in the nearshore. In the absence

871   of bed shear stresses, the depth- and time-averaged momentum equation is (e.g., Mei et al., 2005)

872
$$U\frac{\partial U}{\partial x} = -g\frac{\partial \bar{\eta}}{\partial x} - \frac{1}{\rho(\bar{\eta}+h)}\frac{\partial S_{xx}}{\partial x} \qquad (11)$$

873   where U is the mean (depth and time-averaged) current, $\bar{\eta}$ is the wave setup and S_{xx} is the

874   radiation stress representing the excess momentum flux associated with waves (including

875   turbulence contributions). The response of mean water levels and flow in the nearshore thus depend

876   on how radiation stresses evolve through the surf zone per Equation (11). The radiation stress (S_{xx})

877   can be defined in general form as (e.g., Mei et al., 2005)

878

$$S_{xx} = \overline{\int_{-h}^{\eta} \left(\underbrace{\rho\tilde{u}^2 - \rho\tilde{w}^2}_{\text{wave part}} + \underbrace{\rho\overline{u'^2} - \rho\overline{w'^2}}_{\text{turbulent part}} \right)dz + \frac{1}{2}\rho g\overline{\eta^2}} \tag{12}$$

879   which reveals that it is comprised of terms related to both wave and turbulent velocities, as well as

880   the water level variance. Therefore, a primary challenge in surf zone modelling is how to accurately

881   account for various contributions to radiation stresses in the presence of nonlinear, breaking waves.

882   Phase-averaged wave models are based on linear wave theory (LWT), where the radiation stress is

883   given as

884

$$S_{xx,LWT} = \left(2n - \frac{1}{2} \right)E \tag{13}$$

885   where $n = c_g / c$ represents the ratio of the group (c_g) and phase (c) velocities, $E = \rho g\overline{\eta^2}$ is the

886   energy density with PE and KE contributions being in balance for linear waves. These phase-

887   averaged models are often supplemented by empirical corrections to parameterize nonlinear wave

888   behaviour as well as the rate at which PE is converted to KE and then dissipated within breaking

889   waves (i.e., through use of empirical roller models). Conventional phase-resolving models (e.g.,

890   Boussinesq and non-hydrostatic) resolve the nonlinear wave characteristics that influence radiation

891   stresses; however, they cannot fully resolve the wave breaking processes that can also affect

892   radiation stress estimates (particularly through robust predictions of surf zone turbulent motions).

893   To explore how different components of the radiation stress vary across the surf zone, we

894   decompose the individual terms in Eq. (12) that contribute to the cross-shore variability in S_{xx}

895   during breaking, again using the TK94 spilling case as an illustrative example (Figure 15). The

896   results reveal the significant role that the turbulent contribution plays (following breaking) in

897   shifting the radiation stress gradients shoreward (Figure 15a), and hence the wave forces

898   responsible for generation of wave setup via Eq. (12). While the dominant wave contribution to the

899   radiation stress ($\tilde{u}^2$) decays monotonically during breaking, this triggers a rise in turbulent

900   contribution ($\overline{u'^2}$) that shifts the total (combined) S_{xx} shoreward (Figure 15b). In phase-averaged

901   wave models, as well as depth-averaged phase-resolving models, this delay in wave forces can only

902 be parameterized, which for example, historically motivated the development of roller models to

903 improve predictions of wave setup and wave-driven flows within the surf zone (Svendsen, 1984).

904 The results reveal how the present SPH simulations can incorporate the detailed hydrodynamic

905 processes responsible for generating wave forces within the surf zone, which can explain why the

906 model was able to accurately predict both wave setup and mean current distributions for all test

907 cases considered.

908   We can lastly compare how the radiation stresses (S_{xx}) deviate from linear wave theory

909 (LWT), given that it still forms the basis of coastal-scale wave predictions using phase-averaged

910 models. In particular, following Svendsen and Putrevu (1993) we define the wave parameter P by

911 normalizing the radiation stress as $P = S_{xx}/\rho g H^2$ (Figure 15c), where the wave height H is

912 equivalent to $H = \sqrt{8\overline{\eta^2}}$ (Torres-Freyermuth et al., 2007). Therefore, given that the waves in this

913 example are shallow, LWT holds when $P = 3/16 \approx 0.19$ (as indicated by the horizontal dashed line

914 in Figure 15c). The results indicate that in the shoaling region $P \approx 0.14$, thus significantly lower

915 than LWT would predict; however, following breaking P increases significantly above LWT,

916 reaching values up to $P \approx 0.22$ as a consequence of the enhancement of the radiation stress by surf

917 zone turbulent kinetic energy. These results are very similar to the experimental findings of

918 Svendsen and Putrevu (1993), who examined experimental observations of radiation stresses on

919 mild-sloping plane beaches, and found that P was often much less compared to what LWT would

920 predict during shoaling due to the nonlinear shape of waves (i.e., skewness, associated with the

921 waves having narrow, peaked crests and long, shallow troughs). Similarly, they observed that P

922 reached elevated values following breaking (typically P=0.2-0.3), which is also consistent with the

923 present results.

924

5   Conclusions

926   This study has demonstrated how the mesh-free SPH approach can provide accurate and

927 robust predictions of complex surf zone hydrodynamic processes generated by wave breaking, with

928 model performance comparable to applications of state-of-the-art mesh-based CFD models such as

929 OpenFOAM. Over the wide range of wave breaking types considered, the SPH approach was able

930 to reproduce many of the detailed hydrodynamic processes that govern the nonlinear evolution of

931 wave shape in the nearshore, the free surface characteristics of breaking waves (including violent,

932 plunging waves), the processes governing energy conversion between potential and kinetic energy

933 within the surf zone, and the resulting mean wave-driven flow properties (including wave setup and

934 undertow profiles). A particular advantage of approach used here (the weakly-compressible SPH

935 code DualSPHysics), was its ability to run on computationally-efficient GPUs that enabled high-

936 resolution simulations (sub-millimetre particle spacing) of the experimental results to be achieved

937 on a single-GPU.

938   Given that the performance of the SPH approach was evaluated using common experimental

939 test cases (e.g., TK94) that have been widely-applied to benchmark the performance of other classes

940 of phase-resolving wave-flow models (e.g., Boussinesq, non-hydrostatic, and CFD), the results also

941 provided an opportunity to inter-compare how different defining characteristics of these models

942 may influence model performance. Based on prior model applications to these experimental

943 datasets, it is clear that all of these phase-resolving models (including depth-averaged versions) are

944 fully-capable of accurately resolving the nonlinear evolution of individual waves prior to breaking.

945 However, within the surf zone region, where phase-resolving models cannot directly resolve the

946 overturning free surface, more variable model performance has been reported across the literature.

947 By necessity, depth-averaged versions of these models (e.g., based on Boussinesq and non-

948 hydrostatic approaches) require significant empirical parameterization of the breaking process.

949 Therefore, while these models have often been successful in reproducing surf zone wave

950 transformation, they generally require tuning of empirical parameters (generally on a case-by-case

951 basis), which can undermine their broader predictive utility and may also come at the expense of

952 other hydrodynamic predictions (e.g., degrading that accuracy of wave setup distributions).

953   Mesh-based 3D/2DV models with vertical resolution (e.g., multi-layer non-hydrostatic and

954 CFD models) have been shown in recent years to provide more robust predictions of surf zone wave

955 transformation relative to depth-averaged models, as they are much less dependent on empirical

956 parameterization of the breaking process. Of these models, CFD models based on full solution of

957 the Reynolds Averaged Navier Stokes equations are most analogous to the present SPH simulations

958 as they both can directly resolve overturning breaking waves. In the context of recent applications

959 of high-resolution mesh-based CFD models (i.e., OpenFOAM) that have been applied to the same

960 experimental test cases (e.g., Larsen and Fuhrman, 2018, Brown et al., 2016, Jacobsen et al., 2012),

961 the present results indicate that the SPH approach can reproduce these surf zone processes with

962 comparable skill. In fact, the results of this work suggest that the SPH approach can help to improve

963 predictions within the crest region of breaking waves, as evident by robust predictions of cross-

964 shore mass fluxes and undertow profiles that have been notoriously difficult to predict in mesh-

965 based CFD models. Within the present study, it was also significant to find that the SPH approach

966 was capable of accurately simulating the range of wave breaking conditions across the test cases

967 using a fixed set of model parameters that were consistent with recommended values (i.e.

968 approximately default values within the model). While the range of wave conditions and

969   bathymetry profiles considered are by no means complete in this single study, these findings

970   suggest that the approach can be applied with some confidence for scenarios where experimental

971   data is not available for validation; for example, applied as a valuable tool for designing detailed

972   physical modelling studies or when detailed experimental measurements are not possible to obtain

973   within a study. More broadly, in the context of nearshore wave modelling, arguably the greatest

974   advantage of mesh-free SPH models is also how readily they can deal with complex geometries

975   (bathymetry and topography) that may not readily confirm to a fixed mesh (grid). Therefore, while

976   both SPH and mesh-based CFD models may be used interchangeably in applications with simple

977   nearshore bathymetries (i.e., as in the test cases considered here), the SPH approach may confer

978   some greater practical advantages when simulating nearshore processes with coastal engineering

979   structures or natural bathymetries that form complex geometries.

980   While the present study has demonstrated the great promise of the SPH modelling approach

981   to improving understanding and prediction of surf zone hydrodynamics, it is important to

982   acknowledge that the present focus has been on investigating the performance under simple forcing

983   (i.e., regular waves) and simple bathymetry profiles. This approach was deliberately chosen as an

984   initial starting point to help isolate the performance characteristics of SPH models in the simulation

985   of surf zone hydrodynamics using a simple set of wave breaking conditions. This present work

986   should provide a foundation for further SPH modelling studies of surf zone hydrodynamics under

987   more realistic conditions, including irregular wave conditions and more complicated nearshore

988   bathymetry profiles (e.g., barred beaches, various reef geometries, etc.) where a wealth of

989   experimental data also exists to investigate model performance. While such studies are achievable

990   today, the primary constraint (particularly for irregular wave conditions) is the requirement for

991   much longer simulations (typically more than an order of magnitude greater), and hence

992   computational demand, which is required to properly resolve the statistical properties of irregular

993   waves. For the SPH code used in the present study (DualSPHysics), this greater computational

994   demand could be partially offset by recent developments in coupling the SPH model with efficient

995   phase-resolving wave models (e.g., Altomare et al., 2015b, Altomare et al., 2018, Verbrugghe et al.,

996   2018), thereby concentrating the focus of the SPH simulations on the immediate surf zone region;

997   as well as plans for multi-GPU functionality in future releases of the code.

998   Finally, with SPH applications to coastal problems still in their early stages (certainly in

999   comparison to decades of work using mesh-based models), the many areas of active research and

1000   develop of the SPH approach will help to further advance surf zone applications into the future.

1001   These numerous developments in the SPH approach include, for example, improved boundary

1002   conditions (solid boundaries and at the free surface), inclusion of multi-phase behaviour, enhanced

1003 numerical optimization (including adaptive refinement of particle resolution), and greater accuracy

1004 using approaches such as incompressible SPH (ISPH) (e.g., refer to recent reviews by Violeau and

1005 Rogers (2016) and Gotoh and Khayyer (2018)). One area that deserves attention in future SPH

1006 studies of nearshore wave dynamics is the role of surf zone turbulence, with advanced turbulence

1007 models (sub-particle scale) still being an active area of research. The present study highlights some

1008 interesting attributes of the turbulence fields generated by the breaking waves, but only the 2D

1009 turbulent motions that are directly resolved at the particle scale (albeit at relatively high resolution

1010 in the present study). Future work is required to understand how the incorporation of advanced sub-

1011 turbulent closure schemes and a full description of the 3D dynamics may further improve SPH

1012 predictions of surf zone turbulence and its influence on a range of nearshore hydrodynamic

1013 processes.

1014

1015 **Appendices**

1016 **Appendix A – Model parameter sensitivity**

1017 A number of SPH studies have investigated how various model parameters influence

1018 predictions of the propagation and breaking of waves (e.g., Roselli et al., 2018, González-Cao et al.,

1019 2019, De Padova et al., 2014). We refer the reader to these comprehensive sensitivity analysis

1020 studies for general background on how various model parameters within the WCSPH approach can

1021 influence wave propagation and breaking characteristics. These studies have often focused on the

1022 role of three specific parameters: 1) model resolution, via the initial inter-particle distance (dp); 2)

1023 artificial viscosity (α); and 3) the smoothing coefficient ($coefh$). To explore the influence of these

1024 model parameters on the present results, we initially conducted a sensitivity analysis using the

1025 TK94 spilling case results by varying these parameters over a range of values (dp=2-16 mm, α

1026 =0.002-0.02, and $coefh$=1.0-1.8; Tables A1-A3). From these simulations, we evaluated how the

1027 modelled wave height (H), setup ($\overline{\eta}$) and mean current ($\overline{u}$) patterns compared with the

1028 experimental observations by computing the root-mean-squared error ($RMSE_{\text{expt}}$)

1029
$$RMSE_{\text{expt}} = \sqrt{\frac{\sum_{i=1}^{N}\left(X_{\text{model}} - X_{\text{expt}}\right)^2}{N}}, \qquad (A.1)$$

1030 where X denotes the variable to be compared, N is the total number of data points and the subscripts

1031 'model' and 'expt' denote the predicted and observed results, respectively. For presentation, we

1032 normalize the $RMSE_{\text{expt}}$ by the range in the observed value to compute the normalized root-mean-

1033 squared error ($NRMSE_{\text{expt}}$)

33

$$NRMSE_{\text{expt}} = \frac{RMSE_{\text{expt}}}{X_{\text{expt}}^{\max} - X_{\text{expt}}^{\min}}, \tag{A.2}$$

1034

1035 where the superscripts 'max' and 'min' denote the maximum and minimum values, respectively. To

1036 specifically investigate the convergence behaviour of the model results to dp, we also computed a

1037 second measure of error by using the finest simulation results (dp=2 mm) as the reference data (i.e.

1038 by replacing X_{expt} with X_{fine}) to compute $NRMSE_{\text{fine}}$ using Eqs. (A.1) and (A.2), where the subscript

1039 'fine' denotes the finest resolution results. In this way, the scaling behaviour of model accuracy

1040 with dp becomes decoupled from any potential errors in the experimental measurements.

1041 The raw results of this sensitivity analysis are included in Supplementary Material (Figures

1042 S1-S6) for reference, with the bulk model performance statistics summarised here in Tables A1-A3.

1043 As the particle distance dp decreases, the results converge to the experimental observations (Figure

1044 A1, Table A1) with negligible reductions in $NRMSE_{\text{expt}}$ for $dp\leq3$ mm. Based on this analysis, the

1045 default (finest resolution) simulations can reproduce the experimental measurements with <5%

1046 error for wave height and approximately 10% error for both the setup and mean currents (Table

1047 A1). To assess the convergence behaviour of the numerics alone, on Figure A1 we also include the

1048 response of the $NRMSE_{\text{fine}}$ in which the error is referenced to the finest simulation with (dp=2 mm).

1049 These results indicate that $NRMSE_{\text{fine}}$ decreases as $NRMSE_{fine} \sim dp^{b}$, where a linear regression of the

1050 results in log-log space gives b=1.41, b=1.42, and b=1.0 for wave height, setup and mean current,

1051 respectively (not shown). Note that a number of SPH studies have also investigated how particle

1052 resolution influences model performance in wave applications, often placing the results in the

1053 context of the number of particles resolved within a given incident (offshore) wave height $H_{0,}$

1054 usually with recommendations to keep the ratio H_0/dp greater than order 10 (e.g., Roselli et al.,

1055 2018). The present results indicate that performance gains were rather small for all quantities (wave

1056 heights, setup and currents) when $H_0/dp > 25$ (Table A1).

1057 For all wave applications of SPH using an artificial viscosity α that we are aware of, these

1058 studies have consistently found an optimal value of order 0.01; hence, $\alpha = 0.01$ is defined by

1059 default in DualSPHysics (see section 2.4). A sensitivity analysis was conducted where α was

1060 varied by an order of magnitude to investigate its influence on wave heights, setup and mean

1061 currents (Table A2). The results indicate that all three quantities are insensitive to α over a large

1062 range; only for the lowest value α =0.002 is some deterioration of the results evident. Note that

1063 these results may appear at odds with some studies that have shown a stronger influence of α on

1064 results; namely, De Padova et al. (2014) who investigated the role of α on wave transformation.

1065   However, De Padova et al. (2014) used much coarser resolution (H/dp<5) than in the present study

1066   (H/dp=63), which can likely explain why their results were much more sensitive to α.

1067   Finally, we assessed the role of the smoothing coefficient (*coefh*) on the results (Table A3).

1068   Both the setup and mean current results are mostly insensitive to *coefh* variations over the range

1069   considered (1.0-1.8). However, we observed some small improvements in wave height predictions

1070   for lower values of *coefh*, so *coefh*=1.2 was used in all simulations.

Table A1. Sensitivity analysis and model performance characteristics for simulations with varying initial inter-particle distance (*dp*) for the TK94 spilling case. Note that the * denotes the default *dp* value used within the main study.

dp [mm]	H_0 / *dp*	Particles	Computation time	NRMSE$_{expt}$ [-] Wave height	Setup	Current
2*	62.5	1216373	63.5 hr	0.037	0.091	0.104
3	41.7	544781	23.1 hr	0.036	0.104	0.105
5	25.0	195563	8.1 hr	0.060	0.138	0.111
9	13.9	61556	1.9 hr	0.142	0.199	0.137
14	8.9	25743	1.1 hr	0.177	0.217	0.163

Table A2. Sensitivity analysis of the model results with artificial viscosity (α) for the TK94 spilling case. Note that the * denotes the default α value used within the main study.

α [-]	NRMSE$_{expt}$ Wave height	Setup	Current
0.002	0.119	0.279	0.172
0.006	0.043	0.093	0.100
0.010*	0.037	0.091	0.104
0.015	0.031	0.095	0.097
0.020	0.032	0.097	0.091

Table A3. Sensitivity analysis of the model results with smoothing coefficient (*coefh*) for the TK94 spilling case. Note that the * denotes the default *coefh* value used within the main study.

coefh [-]	NRMSE$_{expt}$ Wave height	Setup	Current
1.0	0.035	0.091	0.100
1.2*	0.037	0.091	0.104
1.4	0.100	0.096	0.134
1.6	0.091	0.101	0.116
1.8	0.094	0.118	0.124

Acknowledgements

References

AKBARI, H. 2017. Simulation of wave overtopping using an improved SPH method. *Coastal Engineering,* 126**,** 51-68.

ALTOMARE, C., CRESPO, A. J., DOMÍNGUEZ, J. M., GÓMEZ-GESTEIRA, M., SUZUKI, T. & VERWAEST, T. 2015a. Applicability of smoothed particle hydrodynamics for estimation of sea wave impact on coastal structures. *Coastal Engineering,* 96**,** 1-12.

ALTOMARE, C., CRESPO, A. J., ROGERS, B., DOMINGUEZ, J., GIRONELLA, X. & GÓMEZ-GESTEIRA, M. 2014. Numerical modelling of armour block sea breakwater with smoothed particle hydrodynamics. *Computers & Structures,* 130**,** 34-45.

ALTOMARE, C., DOMÍNGUEZ, J., CRESPO, A., SUZUKI, T., CACERES, I. & GÓMEZ-GESTEIRA, M. 2015b. Hybridization of the wave propagation model SWASH and the meshfree particle method SPH for real coastal applications. *Coastal Engineering Journal,* 57**,** 1550024-1-1550024-34.

ALTOMARE, C., DOMÍNGUEZ, J. M., CRESPO, A., GONZÁLEZ-CAO, J., SUZUKI, T., GÓMEZ-GESTEIRA, M. & TROCH, P. 2017. Long-crested wave generation and absorption for SPH-based DualSPHysics model. *Coastal Engineering,* 127**,** 37-54.

ALTOMARE, C., TAGLIAFIERRO, B., DOMINGUEZ, J. M., SUZUKI, T. & VICCIONE, G. 2018. Improved relaxation zone method in SPH-based model for coastal engineering applications. *Applied Ocean Research,* 81**,** 15-33.

BATTJES, J. & SAKAI, T. 1981. Velocity field in a steady breaker. *Journal of Fluid Mechanics,* 111**,** 421-437.

BOUSCASSE, B., COLAGROSSI, A., MARRONE, S. & ANTUONO, M. 2013. Nonlinear water wave interaction with floating bodies in SPH. *Journal of Fluids and Structures,* 42**,** 112-129.

BRADFORD, S. F. 2010. Nonhydrostatic model for surf zone simulation. *Journal of Waterway, Port, Coastal, and Ocean Engineering,* 137**,** 163-174.

BREDMOSE, H., SCHÄFFER, H. & MADSEN, P. A. 2004. Boussinesq evolution equations: Numerical efficiency, breaking and amplitude dispersion. *Coastal Engineering,* 51**,** 1117-1142.

BROWN, S. A., GREAVES, D. M., MAGAR, V. & CONLEY, D. C. 2016. Evaluation of turbulence closure models under spilling and plunging breakers in the surf zone. *Coastal Engineering,* 114**,** 177-193.

BUCKLEY, M. L., LOWE, R. J., HANSEN, J. E. & VAN DONGEREN, A. R. 2015. Dynamics of wave setup over a steeply sloping fringing reef. *Journal of Physical Oceanography,* 45**,** 3005-3023.

CHO, Y.-S. 2003. A note on estimation of the Jacobian elliptic parameter in cnoidal wave theory. *Ocean engineering,* 30**,** 1915-1922.

CIENFUEGOS, R., BARTHÉLEMY, E. & BONNETON, P. 2010. Wave-breaking model for Boussinesq-type equations including roller effects in the mass conservation equation. *Journal of Waterway, Port, Coastal, and Ocean Engineering,* 136**,** 10-26.

CRESPO, A., ALTOMARE, C., DOMÍNGUEZ, J., GONZÁLEZ-CAO, J. & GÓMEZ-GESTEIRA, M. 2017. Towards simulating floating offshore oscillating water column converters with smoothed particle hydrodynamics. *Coastal Engineering,* 126**,** 11-26.

CRESPO, A., GÓMEZ-GESTEIRA, M. & DALRYMPLE, R. A. 2007. Boundary conditions generated by dynamic particles in SPH methods. *CMC-TECH SCIENCE PRESS-,* 5**,** 173.

CRESPO, A. C., DOMINGUEZ, J. M., BARREIRO, A., GÓMEZ-GESTEIRA, M. & ROGERS, B. D. 2011. GPUs, a new tool of acceleration in CFD: efficiency and reliability on smoothed particle hydrodynamics methods. *PloS one,* 6**,** e20685.

CRESPO, A. J., DOMÍNGUEZ, J. M., ROGERS, B. D., GÓMEZ-GESTEIRA, M., LONGSHAW, S., CANELAS, R., VACONDIO, R., BARREIRO, A. & GARCÍA-FEAL, O. 2015. DualSPHysics: Open-source parallel CFD solver based on Smoothed Particle Hydrodynamics (SPH). *Computer Physics Communications,* 187**,** 204-216.

DALRYMPLE, R. A. & ROGERS, B. 2006. Numerical modeling of water waves with the SPH method. *Coastal engineering,* 53**,** 141-147.

DE PADOVA, D., BROCCHINI, M., BURIANI, F., CORVARO, S., DE SERIO, F., MOSSA, M. & SIBILLA, S. 2018. Experimental and Numerical Investigation of Pre-Breaking and Breaking Vorticity within a Plunging Breaker. *Water,* 10**,** 387.

DE PADOVA, D., DALRYMPLE, R. A. & MOSSA, M. 2014. Analysis of the artificial viscosity in the smoothed particle hydrodynamics modelling of regular waves. *Journal of Hydraulic Research,* 52**,** 836-848.

DERAKHTI, M., KIRBY, J. T., SHI, F. & MA, G. 2016a. Wave breaking in the surf zone and deep-water in a non-hydrostatic RANS model. Part 1: Organized wave motions. *Ocean Modelling,* 107**,** 125-138.

DERAKHTI, M., KIRBY, J. T., SHI, F. & MA, G. 2016b. Wave breaking in the surf zone and deep-water in a non-hydrostatic RANS model. Part 2: Turbulence and mean circulation. *Ocean Modelling,* 107**,** 139-150.

DEVOLDER, B., RAUWOENS, P. & TROCH, P. 2017. Application of a buoyancy-modified k-ω SST turbulence model to simulate wave run-up around a monopile subjected to regular waves using OpenFOAM®. *Coastal Engineering,* 125**,** 81-94.

DEVOLDER, B., TROCH, P. & RAUWOENS, P. 2018. Performance of a buoyancy-modified k-ω and k-ω SST turbulence model for simulating wave breaking under regular waves using OpenFOAM®. *Coastal Engineering,* 138**,** 49-65.

DOMÍNGUEZ, J., ALTOMARE, C., GONZALEZ-CAO, J. & LOMONACO, P. 2019. Towards a more complete tool for coastal engineering: solitary wave generation, propagation and breaking in an SPH-based model. *Coastal Engineering Journal***,** 1-26.

DOMÍNGUEZ, J. M., CRESPO, A. J. & GÓMEZ-GESTEIRA, M. 2013. Optimization strategies for CPU and GPU implementations of a smoothed particle hydrodynamics method. *Computer Physics Communications,* 184**,** 617-627.

ELDEBERKY, Y. & BATTJES, J. 1995. Nonlinear coupling in waves propagating over a bar. *Coastal Engineering 1994.*

FARAHANI, R. J. & DALRYMPLE, R. A. 2014. Three-dimensional reversed horseshoe vortex structures under broken solitary waves. *Coastal Engineering,* 91**,** 261-279.

FARAHANI, R. J., DALRYMPLE, R. A., HÉRAULT, A. & BILOTTA, G. 2013. Three-dimensional SPH modeling of a bar/rip channel system. *Journal of Waterway, Port, Coastal, and Ocean Engineering,* 140**,** 82-99.

GINGOLD, R. A. & MONAGHAN, J. J. 1977. Smoothed particle hydrodynamics: theory and application to non-spherical stars. *Monthly notices of the royal astronomical society,* 181**,** 375-389.

GONZÁLEZ-CAO, J., ALTOMARE, C., CRESPO, A., DOMÍNGUEZ, J., GÓMEZ-GESTEIRA, M. & KISACIK, D. 2019. On the accuracy of DualSPHysics to assess violent collisions with coastal structures. *Computers & Fluids,* 179**,** 604-612.

GOTOH, H. & KHAYYER, A. 2018. On the state-of-the-art of particle methods for coastal and ocean engineering. *Coastal Engineering Journal,* 60**,** 79-103.

GOTOH, H., SHAO, S. & MEMITA, T. 2004. SPH-LES model for numerical investigation of wave interaction with partially immersed breakwater. *Coastal Engineering Journal,* 46**,** 39-63.

HARLOW, F. H. & WELCH, J. E. 1965. Numerical calculation of time‐dependent viscous incompressible flow of fluid with free surface. *The physics of fluids,* 8**,** 2182-2189.

HATTORI, M. & AONO, T. 1985. Experimental study on turbulence structures under breaking waves. *Coastal Engineering in Japan,* 28**,** 97-116.

HIRT, C. W. & NICHOLS, B. D. 1981. Volume of fluid (VOF) method for the dynamics of free boundaries. *Journal of computational physics,* 39**,** 201-225.

ISSA, R. & VIOLEAU, D. 2009. Modelling a plunging breaking solitary wave with eddy-viscosity turbulent SPH models. *Comput. Mater. Continua,* 8**,** 151-164.

JACOBSEN, N. G. 2011. A full hydro-and morphodynamic description of breaker bar development. *Technical University of Denmark.*

JACOBSEN, N. G., FUHRMAN, D. R. & FREDSØE, J. 2012. A wave generation toolbox for the open-source CFD library: OpenFoam®. *International Journal for Numerical Methods in Fluids,* 70**,** 1073-1088.

KENNEDY, A. B., CHEN, Q., KIRBY, J. T. & DALRYMPLE, R. A. 2000. Boussinesq modeling of wave transformation, breaking, and runup. I: 1D. *Journal of waterway, port, coastal, and ocean engineering,* 126**,** 39-47.

LAKEHAL, D. & LIOVIC, P. 2011. Turbulence structure and interaction with steep breaking waves. *Journal of Fluid Mechanics,* 674**,** 522-577.

LARSEN, B. E. & FUHRMAN, D. R. 2018. On the over-production of turbulence beneath surface waves in Reynolds-averaged Navier–Stokes models. *Journal of Fluid Mechanics,* 853**,** 419-460.

LASHLEY, C. H., ROELVINK, D., VAN DONGEREN, A., BUCKLEY, M. L. & LOWE, R. J. 2018. Nonhydrostatic and surfbeat model predictions of extreme wave run-up in fringing reef environments. *Coastal Engineering,* 137**,** 11-27.

LEE, E. S., MOULINEC, C., XU, R., VIOLEAU, D., LAURENCE, D. & STANSBY, P. 2008. Comparisons of weakly compressible and truly incompressible algorithms for the SPH mesh free particle method. *Journal of Computational Physics,* 227**,** 8417-8436.

LEMMIN, U., SCOTT, J. T. & CZAPSKI, U. H. 1974. The development from two‐dimensional to three‐dimensional turbulence generated by breaking waves. *Journal of Geophysical Research,* 79**,** 3442-3448.

LESIEUR, M. 2008. Two-Dimensional Turbulence. *Turbulence in Fluids: Fourth Revised and Enlarged Edition***,** 311-348.

LIU, G. & LIU, M. 2003. *Smoothed Particle Hydrodynamics*.

LUCY, L. B. 1977. A numerical approach to the testing of the fission hypothesis. *The astronomical journal,* 82**,** 1013-1024.

LYNETT, P. J. 2006. Nearshore wave modeling with high-order Boussinesq-type equations. *Journal of waterway, port, coastal, and ocean engineering,* 132**,** 348-357.

MA, G., SHI, F. & KIRBY, J. T. 2012. Shock-capturing non-hydrostatic model for fully dispersive surface wave processes. *Ocean Modelling,* 43-44**,** 22-35.

MADSEN, P. A., SØRENSEN, O. R. & SCHÄFFER, H. A. 1997. Surf zone dynamics simulated by a Boussinesq type model. Part I. Model description and cross-shore motion of regular waves. *Coastal Engineering,* 32**,** 255-287.

MAKRIS, C. V., MEMOS, C. D. & KRESTENITIS, Y. N. 2016. Numerical modeling of surf zone dynamics under weakly plunging breakers with SPH method. *Ocean Modelling,* 98**,** 12-35.

MEI, C. C., STIASSNIE, M. & YUE, D. K.-P. 2005. *Theory and applications of ocean surface waves: nonlinear aspects*, World scientific.

MOLTENI, D. & COLAGROSSI, A. 2009. A simple procedure to improve the pressure evaluation in hydrodynamic context using the SPH. *Computer Physics Communications,* 180**,** 861-872.

MONAGHAN, J. & KOS, A. 1999. Solitary waves on a Cretan beach. *Journal of waterway, port, coastal, and ocean engineering,* 125**,** 145-155.

MONAGHAN, J. J. 1992. Smoothed particle hydrodynamics. *Annual review of astronomy and astrophysics,* 30**,** 543-574.

MONAGHAN, J. J. 1994. Simulating free surface flows with SPH. *Journal of computational physics,* 110**,** 399-406.

NADAOKA, K., HINO, M. & KOYANO, Y. 1989. Structure of the turbulent flow field under breaking waves in the surf zone. *Journal of Fluid Mechanics,* 204**,** 359-387.

NIELSEN, P. 1992. *Coastal bottom boundary layers and sediment transport*, World scientific.

OSHER, S. & SETHIAN, J. A. 1988. Fronts propagating with curvature-dependent speed: algorithms based on Hamilton-Jacobi formulations. *Journal of computational physics,* 79**,** 12-49.

REN, B., HE, M., LI, Y. & DONG, P. 2017. Application of smoothed particle hydrodynamics for modeling the wave-moored floating breakwater interaction. *Applied Ocean Research,* 67**,** 277-290.

RIJNSDORP, D. P., SMIT, P. B., ZIJLEMA, M. & RENIERS, A. J. 2017. Efficient non-hydrostatic modelling of 3D wave-induced currents using a subgrid approach. *Ocean Modelling,* 116**,** 118-133.

ROEBER, V., CHEUNG, K. F. & KOBAYASHI, M. H. 2010. Shock-capturing Boussinesq-type model for nearshore wave processes. *Coastal Engineering,* 57**,** 407-423.

ROSELLI, R. A. R., VERNENGO, G., ALTOMARE, C., BRIZZOLARA, S., BONFIGLIO, L. & GUERCIO, R. 2018. Ensuring numerical stability of wave propagation by tuning model parameters using genetic algorithms and response surface methods. *Environmental Modelling & Software,* 103**,** 62-73.

ROSELLI, R. A. R., VERNENGO, G., BRIZZOLARA, S. & GUERCIO, R. 2019. SPH simulation of periodic wave breaking in the surf zone-A detailed fluid dynamic validation. *Ocean Engineering,* 176**,** 20-30.

RUESSINK, B., RAMAEKERS, G. & VAN RIJN, L. 2012. On the parameterization of the free-stream non-linear wave orbital motion in nearshore morphodynamic models. *Coastal Engineering,* 65**,** 56-63.

SCHÄFFER, H. A., MADSEN, P. A. & DEIGAARD, R. 1993. A Boussinesq model for waves breaking in shallow water. *Coastal Engineering,* 20**,** 185-202.

SHAO, S. & JI, C. 2006. SPH computation of plunging waves using a 2‑D sub‑particle scale (SPS) turbulence model. *International Journal for numerical methods in fluids,* 51**,** 913-936.

SKOTNER, C. & APELT, C. J. 1999. Application of a Boussinesq model for the computation of breaking waves: Part 2: Wave-induced setdown and setup on a submerged coral reef. *Ocean Engineering,* 26**,** 927-947.

SMIT, P., JANSSEN, T., HOLTHUIJSEN, L. & SMITH, J. 2014. Non-hydrostatic modeling of surf zone wave dynamics. *Coastal Engineering,* 83**,** 36-48.

SMIT, P., ZIJLEMA, M. & STELLING, G. 2013. Depth-induced wave breaking in a non-hydrostatic, near-shore wave model. *Coastal Engineering,* 76**,** 1-16.

ST-GERMAIN, P., NISTOR, I., TOWNSEND, R. & SHIBAYAMA, T. 2013. Smoothed-particle hydrodynamics numerical modeling of structures impacted by tsunami bores. *Journal of Waterway, Port, Coastal, and Ocean Engineering,* 140**,** 66-81.

STANSBY, P. K. & FENG, T. 2005. Kinematics and depth-integrated terms in surf zone waves from laboratory measurement. *Journal of Fluid Mechanics,* 529**,** 279-310.

SVENDSEN, I. A. 1984. Wave heights and set-up in a surf zone. *Coastal Engineering,* 8**,** 303-329.

SVENDSEN, I. A. & PUTREVU, U. 1993. Surf zone wave parameters from experimental data. *Coastal engineering,* 19**,** 283-310.

TING, F. C. & KIRBY, J. T. 1994. Observation of undertow and turbulence in a laboratory surf zone. *Coastal Engineering,* 24**,** 51-80.

TING, F. C. & KIRBY, J. T. 1995. Dynamics of surf-zone turbulence in a strong plunging breaker. *Coastal Engineering,* 24**,** 177-204.

TING, F. C. & KIRBY, J. T. 1996. Dynamics of surf-zone turbulence in a spilling breaker. *Coastal Engineering,* 27**,** 131-160.

TISSIER, M., BONNETON, P., MARCHE, F., CHAZEL, F. & LANNES, D. 2012. A new approach to handle wave breaking in fully non-linear Boussinesq models. *Coastal Engineering,* 67**,** 54-66.

TONELLI, M. & PETTI, M. 2010. Finite volume scheme for the solution of 2D extended Boussinesq equations in the surf zone. *Ocean Engineering,* 37**,** 567-582.

TORRES‑FREYERMUTH, A., LOSADA, I. J. & LARA, J. L. 2007. Modeling of surf zone processes on a natural beach using Reynolds‑Averaged Navier‑Stokes equations. *Journal of Geophysical Research: Oceans,* 112.

VERBRUGGHE, T., DOMÍNGUEZ, J., ALTOMARE, C., TAFUNI, A., VACONDIO, R., TROCH, P. & KORTENHAUS, A. 2019a. Non-linear wave generation and absorption using open boundaries within DualSPHysics. *Computer Physics Communications*.

VERBRUGGHE, T., DOMÍNGUEZ, J. M., CRESPO, A. J. C., ALTOMARE, C., STRATIGAKI, V., TROCH, P. & KORTENHAUS, A. 2018. Coupling methodology for smoothed particle hydrodynamics modelling of non-linear wave-structure interactions. *Coastal Engineering,* 138**,** 184-198.

VERBRUGGHE, T., STRATIGAKI, V., ALTOMARE, C., DOMÍNGUEZ, J. M., TROCH, P. & KORTENHAUS, A. 2019b. Implementation of Open Boundaries within a Two-Way Coupled SPH Model to Simulate Nonlinear Wave–Structure Interactions. *Energies,* 12**,** 697.

VIOLEAU, D. & ROGERS, B. D. 2016. Smoothed particle hydrodynamics (SPH) for free-surface flows: past, present and future. *Journal of Hydraulic Research,* 54**,** 1-26.

WEI, Z. & DALRYMPLE, R. A. 2018. SURF ZONE WAVE HEATING BY ENERGY DISSIPATION OF BREAKING WAVES. *Coastal Engineering Proceedings,* 1**,** 2.

WEI, Z., DALRYMPLE, R. A., XU, M., GARNIER, R. & DERAKHTI, M. 2017. Short‐crested waves in the surf zone. *Journal of Geophysical Research: Oceans,* 122**,** 4143-4162.

WEI, Z., LI, C., DALRYMPLE, R. A., DERAKHTI, M. & KATZ, J. 2018. Chaos in breaking waves. *Coastal Engineering,* 140**,** 272-291.

WENDLAND, H. 1995. Piecewise polynomial, positive definite and compactly supported radial functions of minimal degree. *Advances in computational Mathematics,* 4**,** 389-396.

YAO, Y. 2012. *Dynamics of water waves over fringing coral reefs.* PhD thesis, Nanyang Technological University, Singapore.

YAO, Y., HE, T., DENG, Z., CHEN, L. & GUO, H. 2019. Large eddy simulation modeling of tsunami-like solitary wave processes over fringing reefs. *Nat. Hazards Earth Syst. Sci.,* 19**,** 1281-1295.

YAO, Y., HUANG, Z., MONISMITH, S. G. & LO, E. Y. 2012. 1DH Boussinesq modeling of wave transformation over fringing reefs. *Ocean Engineering,* 47**,** 30-42.

ZHANG, F., CRESPO, A., ALTOMARE, C., DOMÍNGUEZ, J., MARZEDDU, A., SHANG, S.-P. & GÓMEZ-GESTEIRA, M. 2018a. DualSPHysics: A numerical tool to simulate real breakwaters. *Journal of Hydrodynamics,* 30**,** 95-105.

ZHANG, S., ZHU, L. & LI, J. 2018b. Numerical Simulation of Wave Propagation, Breaking, and Setup on Steep Fringing Reefs. *Water,* 10**,** 1147.

ZHOU, Z., SANGERMANO, J., HSU, T.-J. & TING, F. C. K. 2014. A numerical investigation of wave-breaking-induced turbulent coherent structure under a solitary wave. *Journal of Geophysical Research: Oceans,* 119**,** 6952-6973.

ZIJLEMA, M., STELLING, G. & SMIT, P. 2011. SWASH: An operational public domain code for simulating wave fields and rapidly varied flows in coastal waters. *Coastal Engineering,* 58**,** 992-1012.

ZIJLEMA, M. & STELLING, G. S. 2008. Efficient computation of surf zone waves using the nonlinear shallow water equations with non-hydrostatic pressure. *Coastal Engineering,* 55**,** 780-790.

Figures
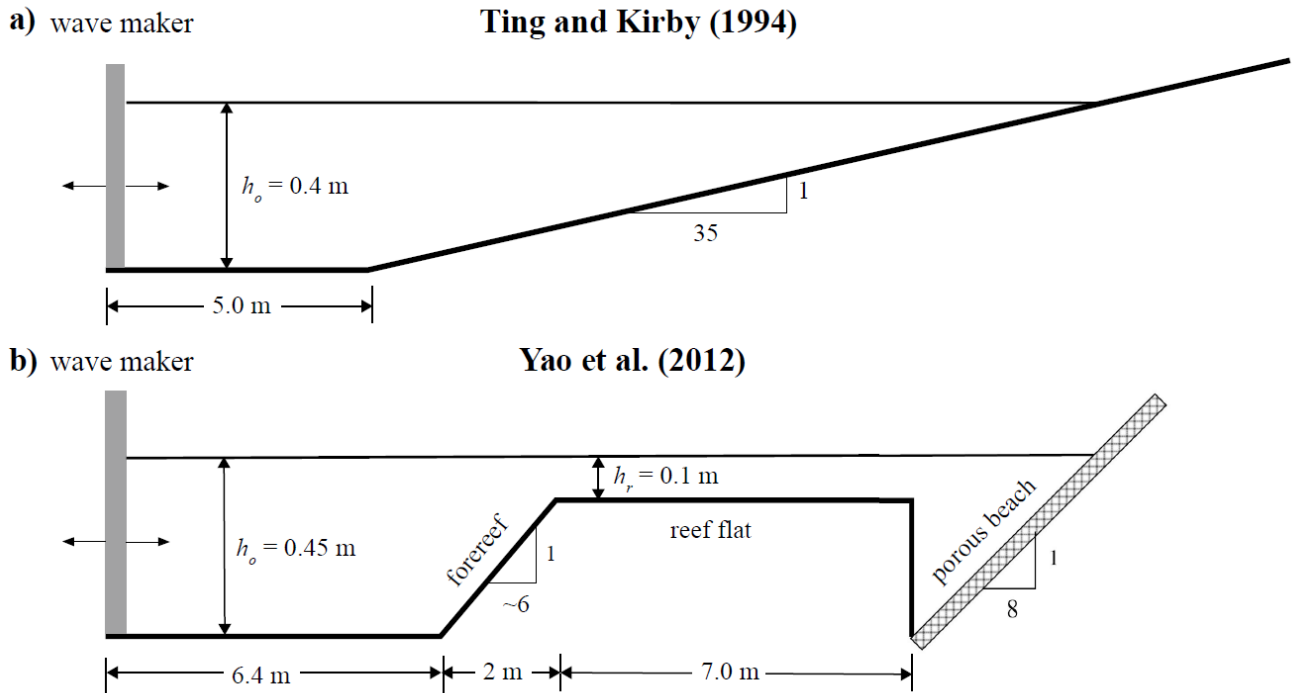
Figure 1. Experimental setup as simulated in the model for the a) Ting and Kirby (1994) and b) Yao et al. (2012) test cases. In both cases, the flat offshore region was shortened for computational efficiency (see text for details). The Yao et al. (2012) case is specifically drawn for Case 1 where h_r=0.1 m. Note that the vertical scale is exaggerated by 8:1.
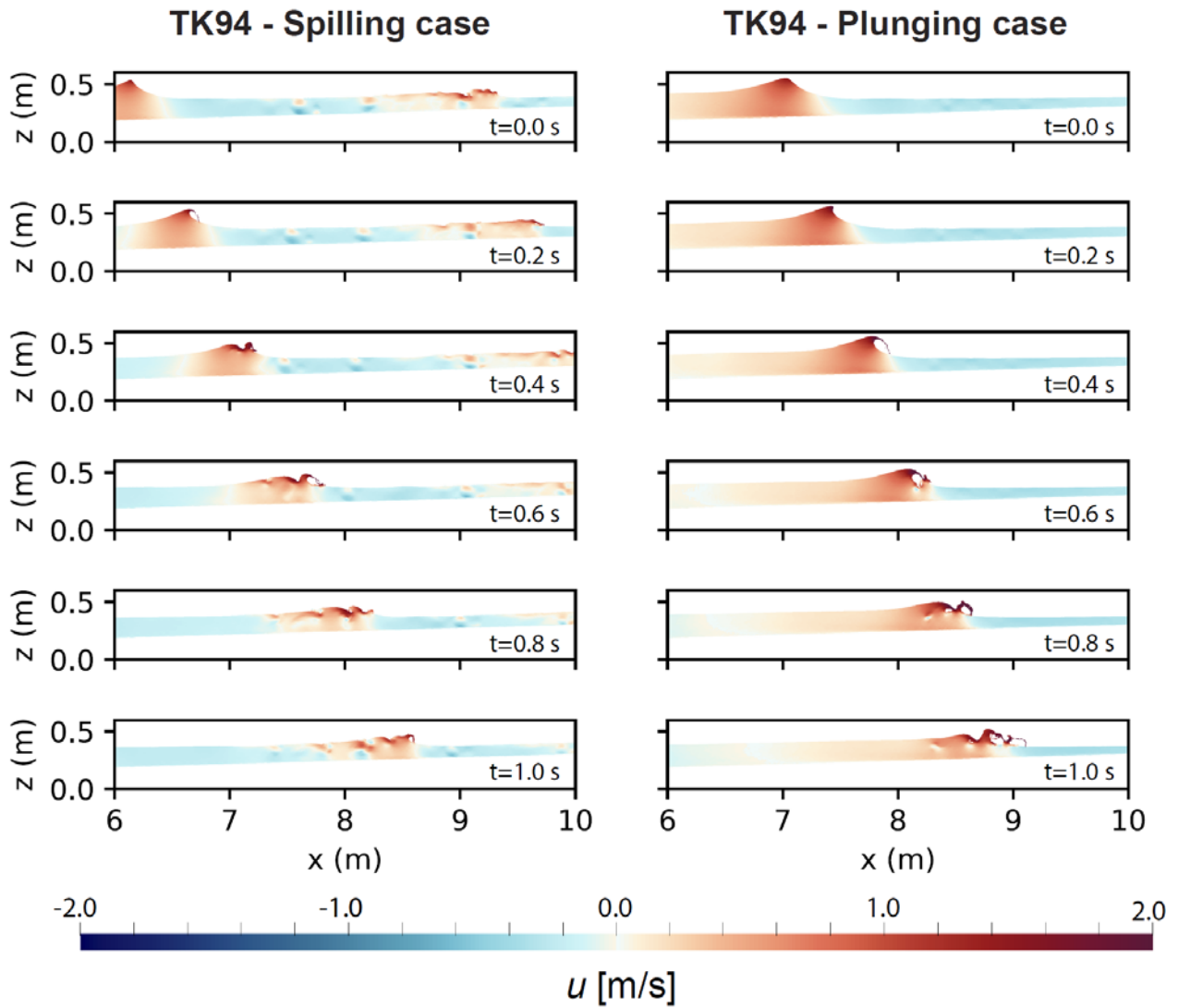
Figure 2. Evolution of wave breaking on a plane beach from TK94 with colours denoting the horizontal (u) velocity component. (Left) spilling case. (Right) plunging case. In both cases the velocity output is displayed at 0.2 s interval, where time t=0 s is arbitrarily assigned to the first figure in the sequence. Note that due to the shorter period (wave length) in the spilling case, two individual waves are visible within the domain shown.
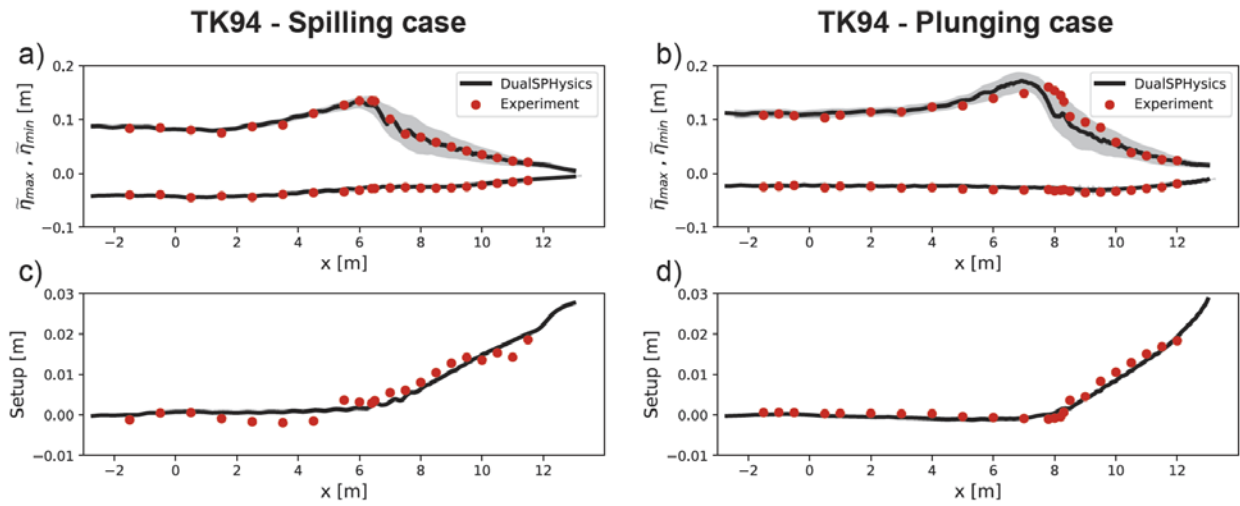
Figure 3. Wave height envelope and wave setup evolution for the (Left column) spilling wave case and (Right column) plunging wave case in TK94. (Top row) envelope of the maximum crest elevation ($\tilde{\eta}_{\max}$) and minimum trough elevation ($\tilde{\eta}_{\min}$) derived from the wave ensemble-averaged water levels. (Bottom row) wave setup. Grey regions denote one standard deviation of the water elevations from the ensemble (wave) average. Note that the standard deviation of the trough elevation is much smaller than the crest elevation, and hence not visible.
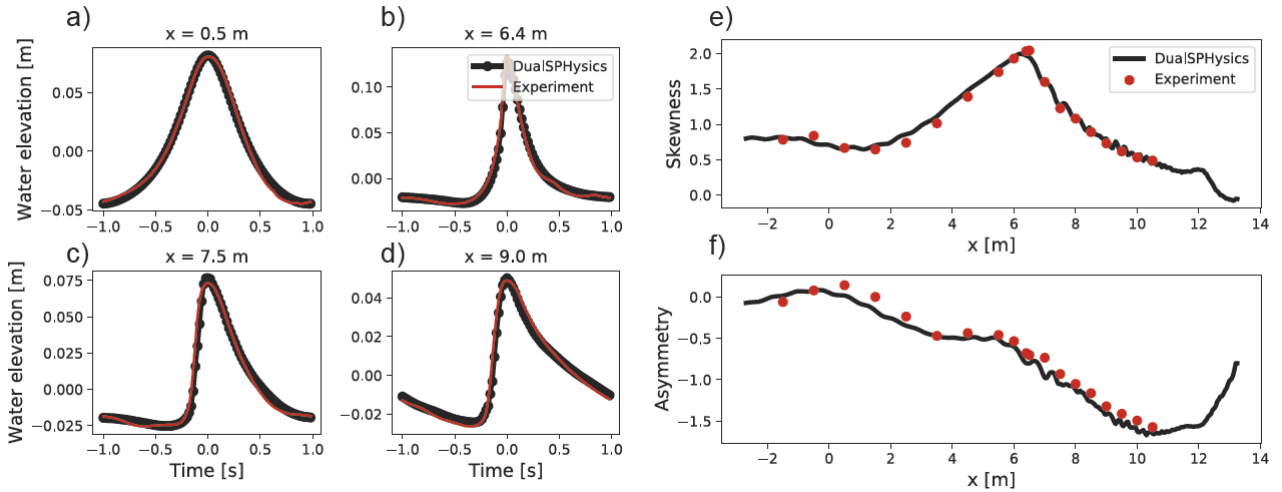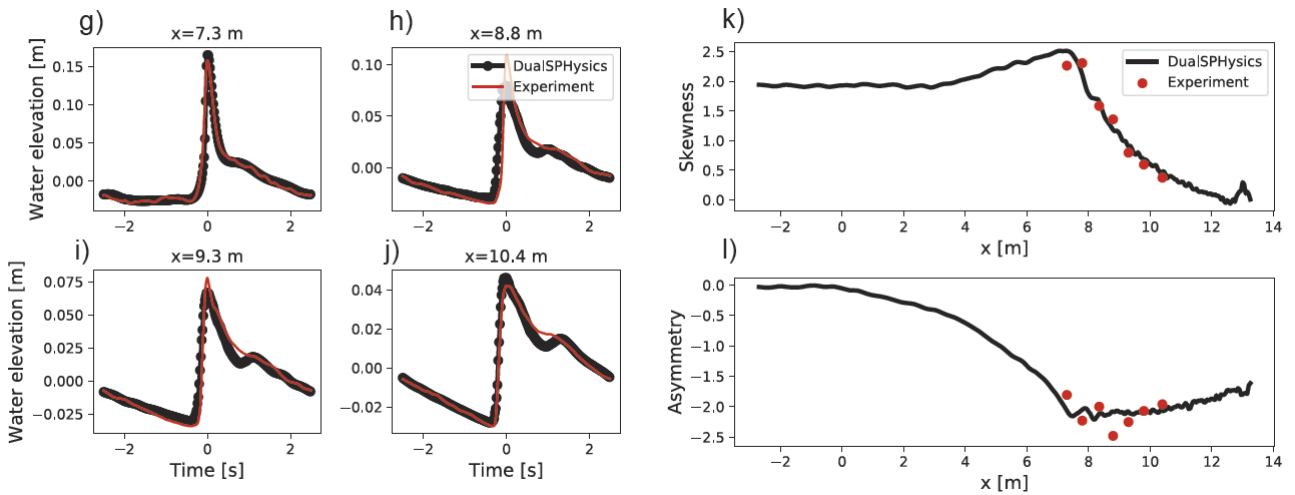
Figure 4. Water surface elevation (wave ensemble-averaged) and wave shape (skewness and asymmetry) evolution for the TK94 experiments. (Top set of panels) spilling case. (Bottom set of panels) plunging case. Note that *t*=0 s is referenced to the time of maximum water level at a given location.
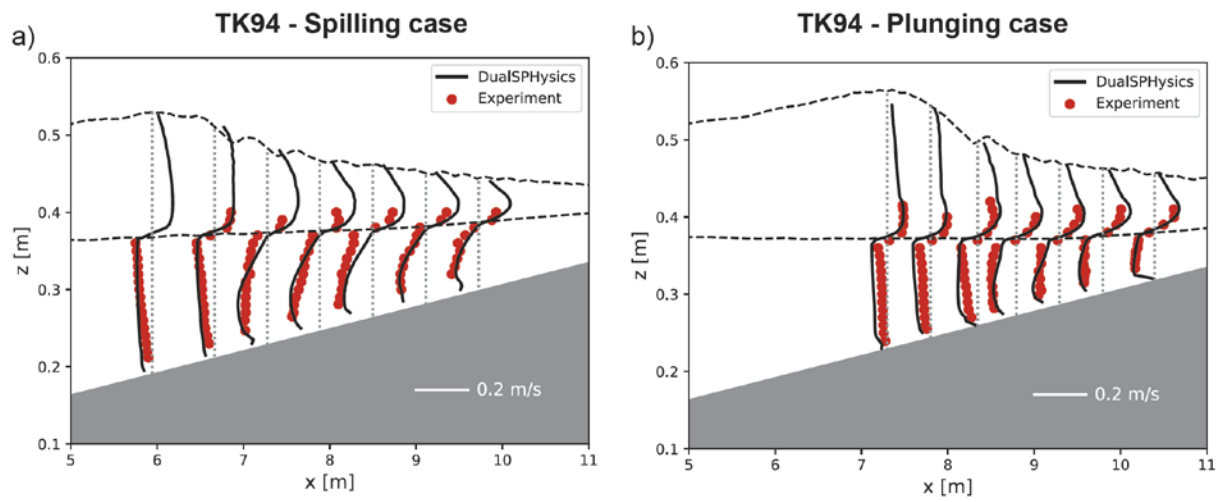
Figure 5. Cross-shore horizontal mean current (*u*) profiles for the a) spilling and b) plunging wave cases in TK94. The horizontal dashed lines denote the ensemble averaged crest and trough elevations. The vertical dotted lines coincide with *u*=0.
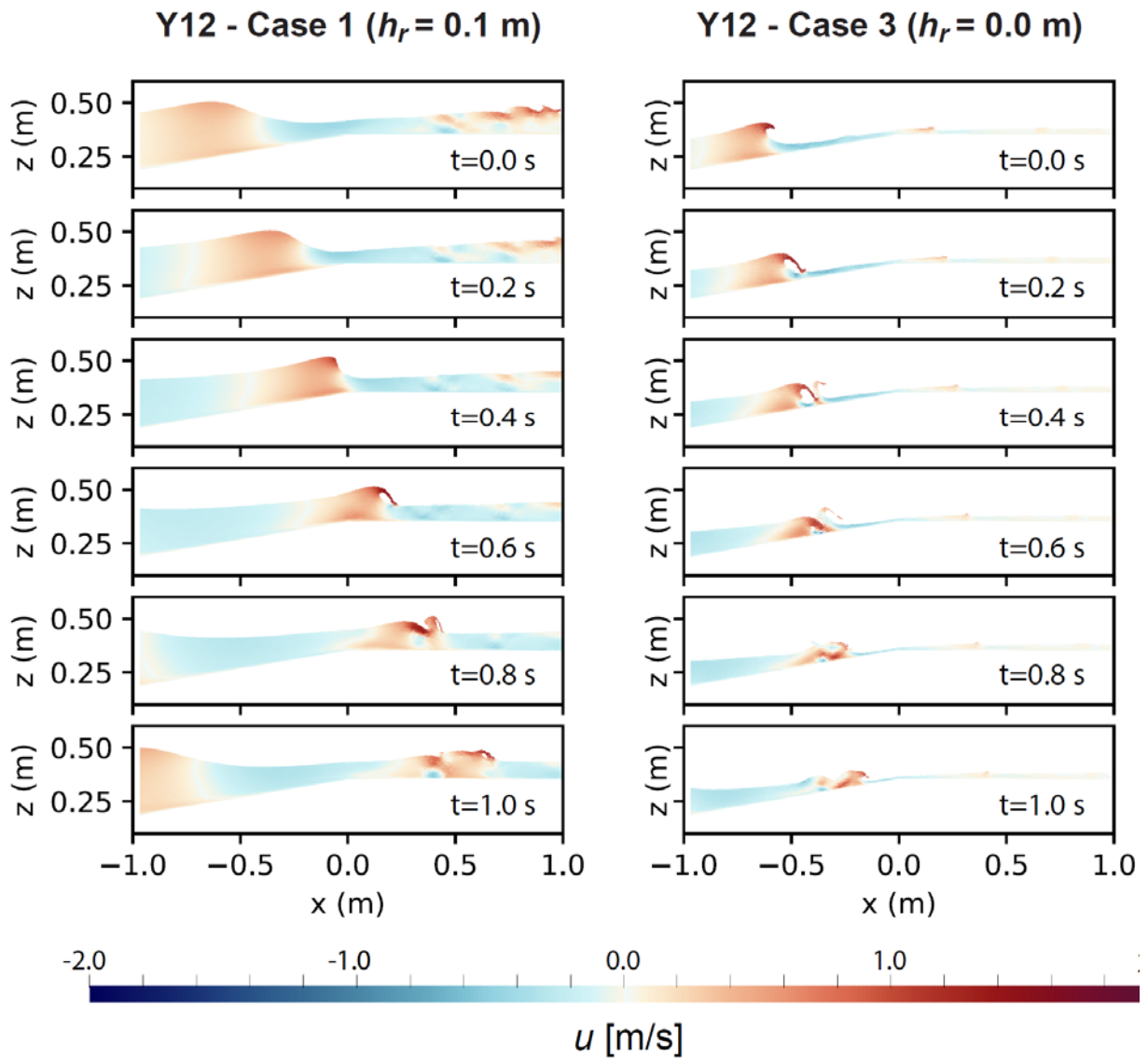
Figure 6. Wave breaking on a plane beach from Y12 with colours denoting the horizontal (u) velocity component. (Left column) Case 1 with h_r=0.1 m. (Right column) Case 3 with h_r=0.0 m. In both cases the velocity output is displayed at 0.2 s interval, where time t=0 s is arbitrarily assigned to the first figure in the sequence.
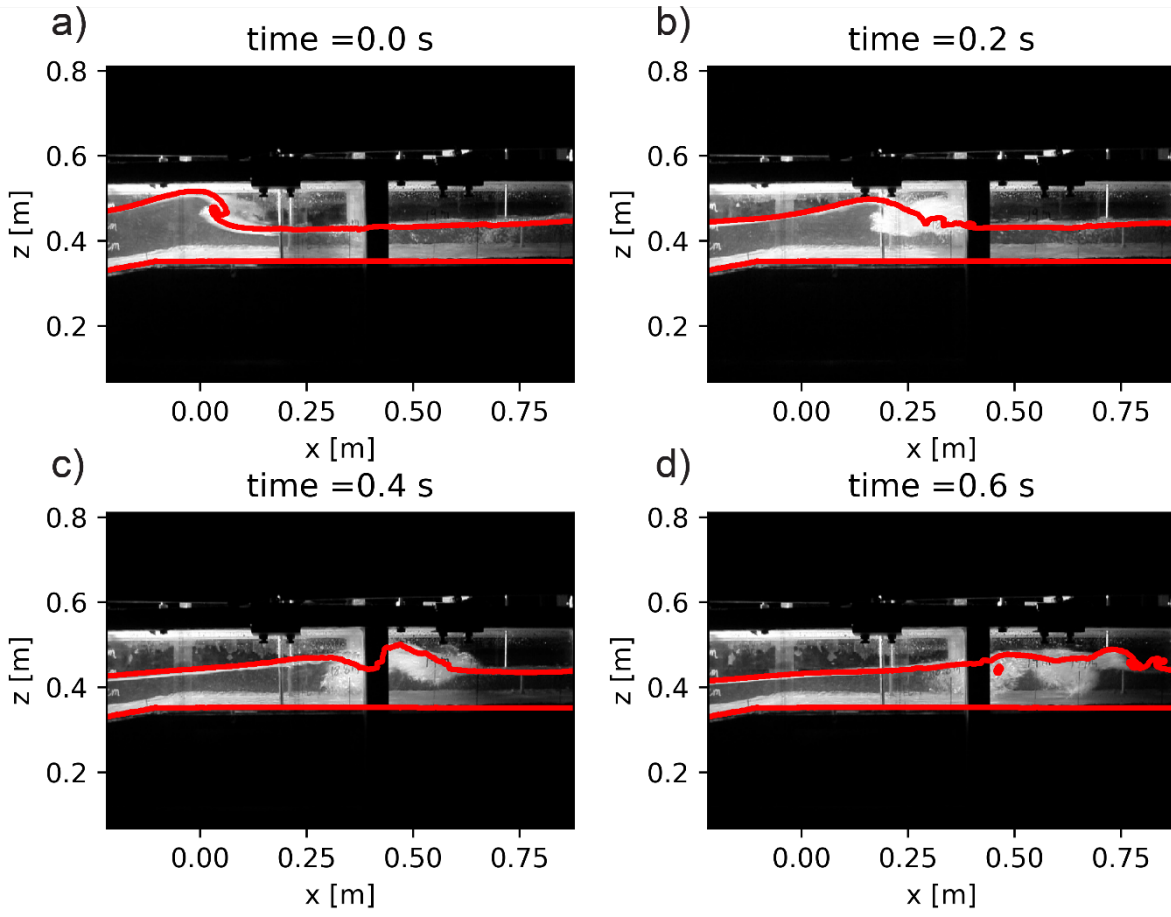
Figure 7. Wave breaking sequence Case 1 of Y12 with the modelled free surface profile superimposed, plotted at 0.2 second intervals.
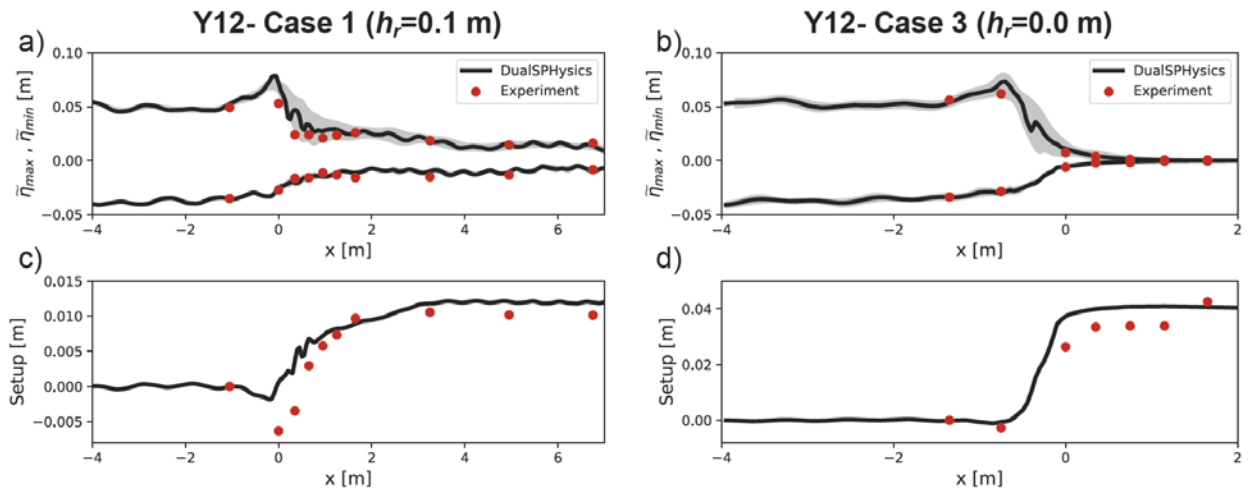
Figure 8. Wave height envelope and wave setup evolution for the two Y12 fringing reef cases. (Left column) Case 1 with h_r=0.1 m. (Right column) Case 3 with h_r=0.0 m. (Top row) envelope of the maximum crest elevation ($\tilde{\eta}_{max}$) and minimum trough elevation ($\tilde{\eta}_{min}$) derived from the wave ensemble-averaged water levels. (Bottom row) wave setup. Grey regions denote one standard deviation of the water elevations from the ensemble (wave) average.

Figure 9. Water surface elevation (wave ensemble-averaged) and wave shape (skewness and asymmetry) evolution over the fringing reef for Y12. (Top set of panels) Case 1 with h_r=0.1 m. (Bottom set of panels) Case 3 with h_r=0.0 m. Note that t=0 s is referenced to the time of maximum water level at a given location.
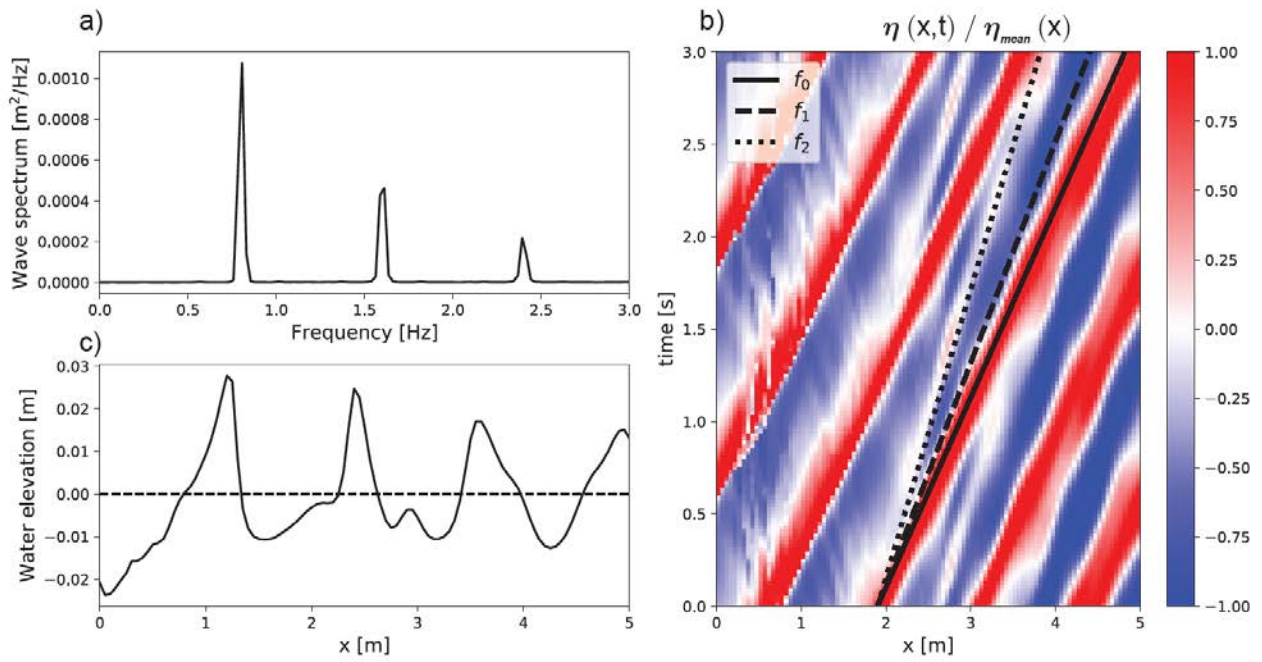
Figure 10. a) Wave spectrum on the reef flat ($x=2$ m). b) Timeseries of the instantaneous water levels across the reef flat over a 3 second period, normalized by the mean wave amplitude at each location $\eta_{mean} \equiv \left(\left| \tilde{\eta}_{max} \right| + \left| \tilde{\eta}_{min} \right| \right) / 2$. The three curves denote the estimated wave paths based on linear wave celerity for the incident wave (f_0) and the first two super-harmonics (f_1 and f_2). c) Water elevation plotted across the reef based on the wave ensemble-averaged elevation $\tilde{\eta}$ (plotted at arbitrary phase) showing the change in wave shape across the reef.
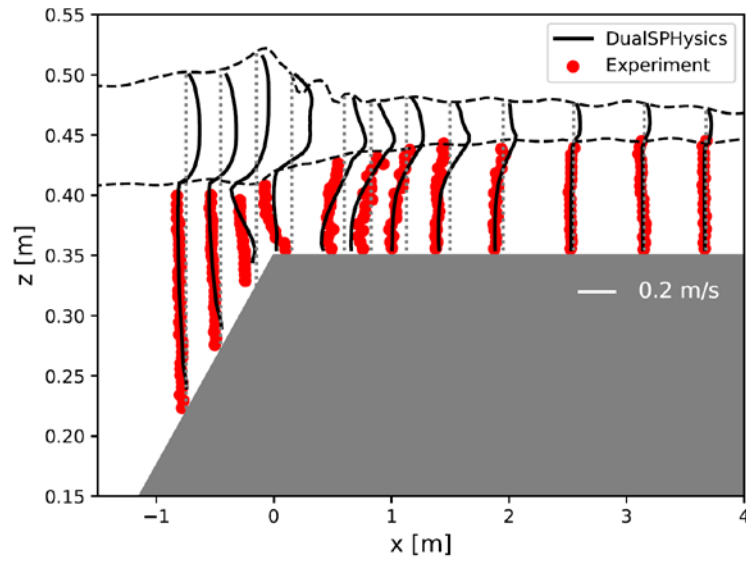
Figure 11. Cross-shore horizontal mean current (*u*) profiles for Case 1 in Y12. The horizontal dashed lines denote the ensemble averaged crest and trough elevations. The vertical dotted lines coincide with *u*=0.
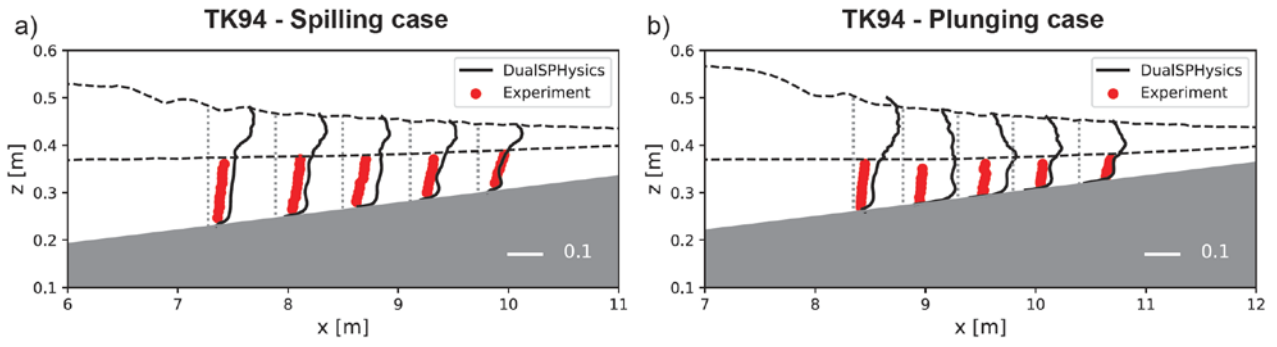
Figure 12. Normalized mean turbulent kinetic energy profiles ($\overline{k}_t^{1/2} / c$) for the a) spilling and b) plunging cases in TK94. Each vertical dotted line denotes the measurement location for comparison, where $\overline{k}_t^{1/2} / c = 0$.
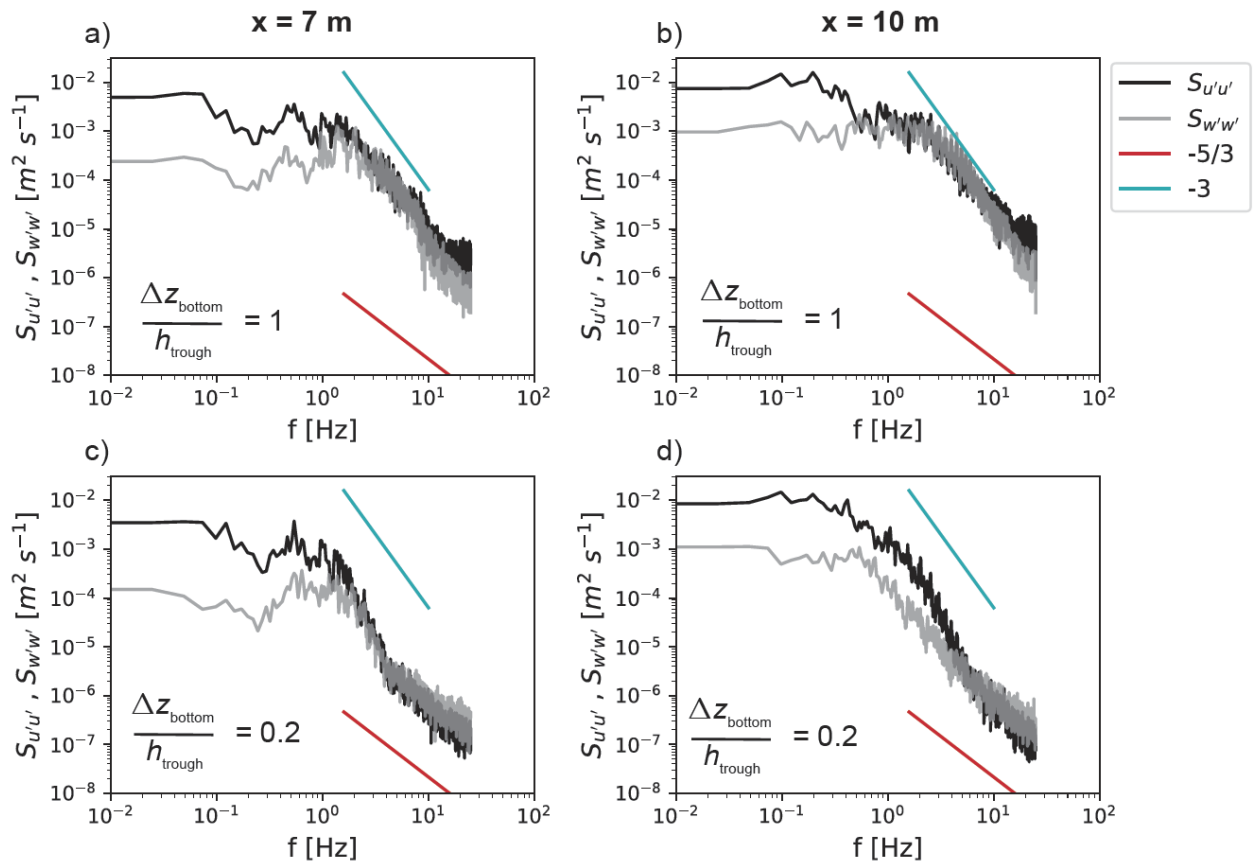
Figure 13. Turbulent velocity spectra for horizontal component $S_{u'u'}$ and vertical component $S_{w'w'}$ at locations within the outer surf zone (x=7 m; left column) and inner surf zone (x=10 m; right column) at two vertical locations coinciding with the trough elevation (top row) and near the bottom (bottom row). Note that the -3 slope (red) and -5/3 slope (blue) in log-log space are shown in arbitrary locations to support visual assessment of trends in the data.
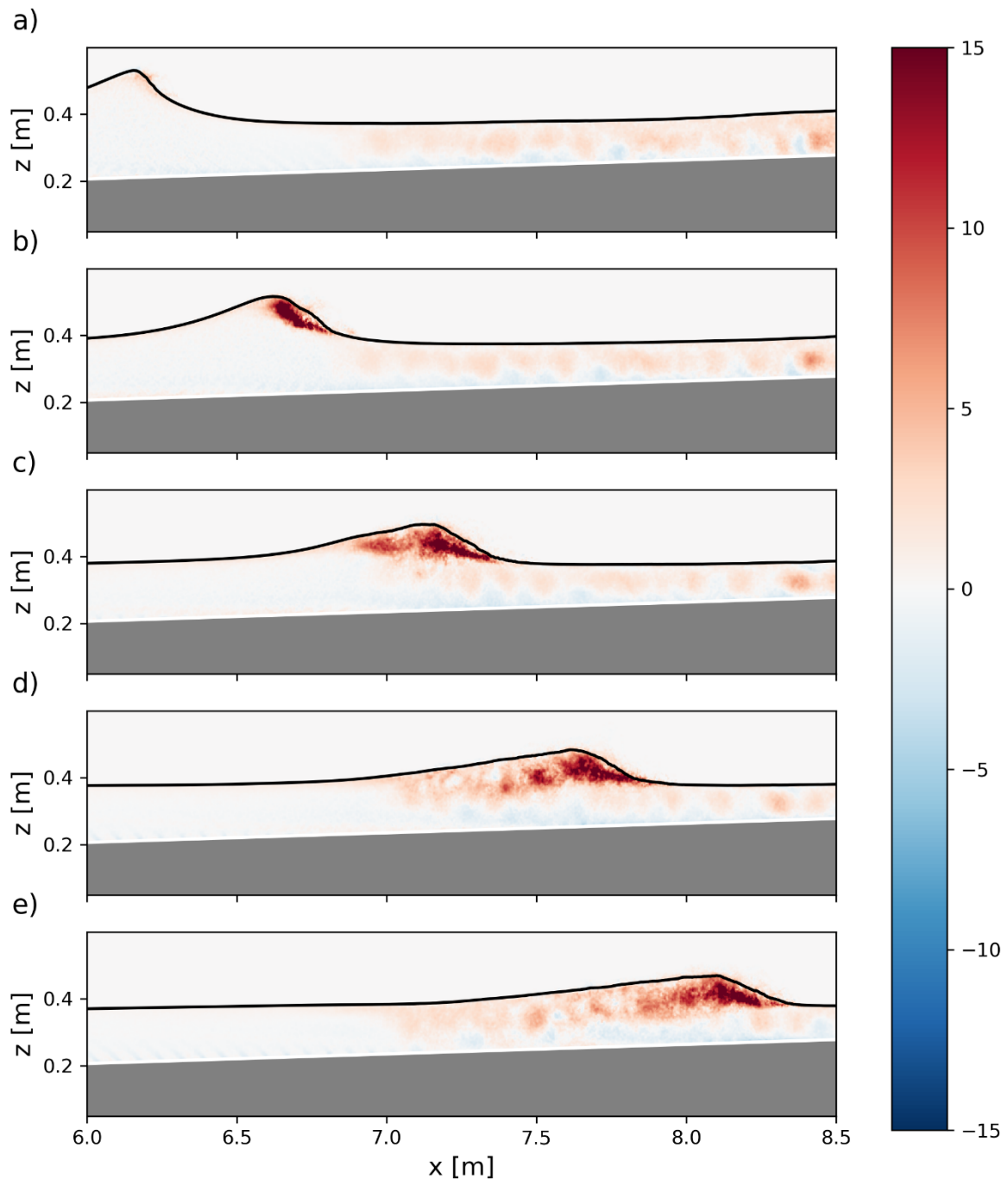
Figure 14. Phase-averaged vorticity [s⁻¹] for the spilling case of TK94, plotted at 0.3 second interval within the surf zone region. Note that colorbar values exceeding the range +/- 15 s⁻¹ are capped at these limiting values and a sign convention is used where positive values represent clockwise motions.
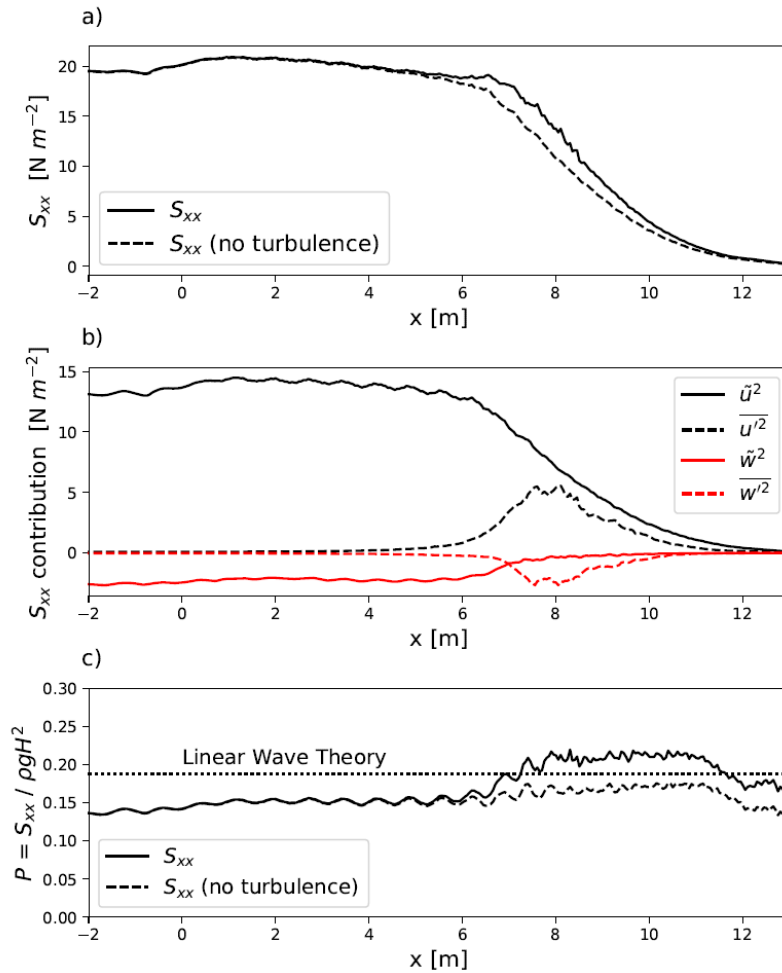
Figure 15. a) Cross-shore distributions of radiation stresses for the spilling case in TK94 with and without turbulence contributions included. b) Individual contributions to the radiation stresses in Eq. (12). c) Ratio of radiation stresses to $\rho g H^2$ (where the ratio equals 3/16 for linear waves) for cases with and without the turbulence contribution to radiation stresses included.
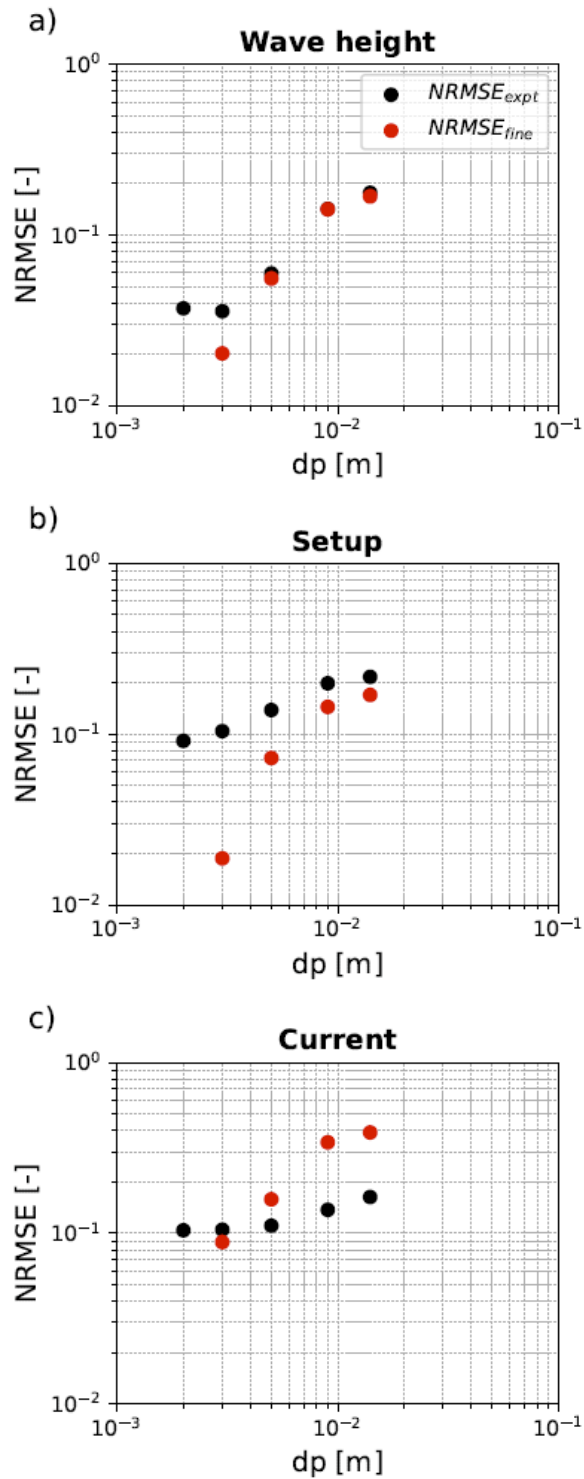
Figure A1. Convergence behaviour of the normalised root mean squared error (NRMSE) with varying initial inter-particle distance (*dp*) through comparison of the a) wave heights, b) setup d, and c) mean current profiles. *NRMSE*_{*expt*} (black dots) and *NRMSE*_{*fine*} (red dots) denote the NRMSE calculated using Eq. (A.2) by referencing the model predictions against the experimental data and finest resolution results (*dp*=0.002 mm), respectively.